FRONT MATTER

A Wearable Freestanding Electrochemical Sensing System

Authors

Y. Zhao[1,2†], B. Wang[1†], H. Hojaiji[1], Z. Wang[1], S. Lin[1], C. Yeung[1,2], H. Lin[1], P. Nguyen[1,3], K. Chiu[1,3], K. Salahi[1], X. Cheng[1,2], J. Tan[1,2], B. A. Cerrillos[1], S. Emaminejad[1*]

Affiliations

[1]Department of Electrical and Computer Engineering, University of California, Los Angeles, CA, USA.
[2]Department of Materials Science and Engineering, University of California, Los Angeles, CA, USA.
[3]College of Letters and Sciences, University of California, Los Angeles, CA, USA.
[*]Correspondence and requests for materials should be addressed to S.E. (emaminejad@ucla.edu)

Abstract

To render high fidelity wearable biomarker data, understanding and engineering the information delivery pathway from epidermally-retrieved biofluid to a readout unit is critical. By examining the biomarker information delivery pathway and recognizing near-zero strained regions within a microfluidic device, a strain-isolated pathway to preserve biomarker data fidelity is engineered. Accordingly, a generalizable and disposable freestanding electrochemical sensing system (FESS) is devised, which simultaneously facilitates sensing and out-of-plane signal interconnection with the aid of double-sided adhesion. The FESS serves as a foundation to realize a system-level design strategy, addressing the challenges of wearable biosensing, in the presence of motion, and integration with consumer electronics. To this end, a FESS-enabled smartwatch was developed, featuring sweat sampling, electrochemical sensing, and data display/transmission, all within a self-contained wearable platform. The FESS-enabled smartwatch was used to monitor the sweat metabolite profiles of individuals in sedentary and high-intensity exercise settings.

MAIN TEXT

Introduction

Leveraging the Internet-of-Things (IoT) infrastructure to transform personalized and precision medicine necessitates the large-scale deployment of health and wellness monitoring sensors in readily-proliferated wearable consumer electronics to harvest physiologically relevant data with minimal user intervention (*1, 2*). To this end, physical sensors have been widely incorporated within commercialized wearable platforms to track the users' physical activities and vital signs (*3-7*). However, to gain insight into the body's dynamic chemistry, electrochemical sensing interfaces are required to target the biomarker molecules present in non-invasively retrieved biofluids such as sweat. To this end, enzymatic, ion-selective, and electroactive electrochemical sensing interfaces were previously developed to target informative analytes such as metabolites and electrolytes (*8-13*). Such sensing interfaces were embedded within sophisticated epidermal microfluidic configurations (*11*) and interfaced with wireless circuit boards to achieve system-level functionality (*14, 15*). However, such implementations, for the most part, focused on optimizing the individual modules separately. Existing systems rely on in-plane interconnections and rigid connectors, fundamentally forcing them to route the transduced

signal from the sensor to the readout electronics through highly strained (motion-induced) regions (*16-18*). This limitation makes them severely susceptible to device operation failure (due to delamination, slipping, detachment, metal interconnect cracking, *etc*.) and external interference (*e.g*., mechanical noise), both of which lead to the loss of data fidelity (*19, 20*). Body motion restriction and/or external fixtures were required to stabilize and communicate the readings, making reported techniques impractical for the envisioned wearable applications.

To achieve high fidelity biomarker data acquisition, careful understanding and subsequently engineering the information delivery pathway from the skin to a readout unit is critical. Unlike the wearable physical sensors harvesting information from direct contact with the epidermis, the electrochemical sensors need to directly interact with the epidermally-retrieved biofluid to target biomarker data. This difference in the target information medium fundamentally necessitates a different design rationale and methodology. As shown in Fig. 1A, for electrochemical sensing, the information delivery pathway consists of sampling and delivering the biomarker-rich biofluid to the sensor surface within a microfluidic structure, followed by signal transduction at the sensor surface and signal routing to the readout electronics via interconnecting elements (*e.g*., metal traces and sensor-circuit connector). To preserve the fidelity of the biomarker information, the signal must be preserved along this pathway in the presence of motion-induced strain.

Here, by examining the biomarker information delivery pathway and recognizing near-zero strained regions within a microfluidic-based sensing module (*21, 22*), we engineer a strain-isolated pathway to preserve the biomarker data fidelity. Accordingly, a generalizable and disposable freestanding electrochemical sensing system (FESS) is devised, which simultaneously facilitates sensing and out-of-plane signal interconnection with the aid of double-sided adhesion. The FESS can be simultaneously adhered to skin and electronics with the aid of double-sided adhesion forces and without the need for rigid connectors. As a standalone unit, the FESS samples and directs epidermally-retrieved biofluids (*e.g*., sweat) for electrochemical sensing. Then, it routes the transduced signal to the readout electronics through a strain-isolated pathway with the aid of out-of-plane interconnection.

On a broader scope, the FESS can serve as a foundation to realize an unprecedented system-level design strategy to address the challenges of wearable biosensing and integration with consumer electronics for daily use. To illustrate this point, the FESS was integrated within a custom-developed smartwatch to render a self-contained and skin-mountable wearable platform capable of sweat induction, sampling, electrochemical sensing, signal processing, and data display/transmission. The FESS-enabled smartwatch was specifically employed to monitor the sweat metabolite profiles of individuals engaged in various daily activities. The results indicate that the devised FESS-enabled platform renders high fidelity signal transduction as well as robust mechanical contact with human skin without constraining user motion. This freestanding sensing system can be integrated with the future wearable consumer electronics to generate high-fidelity longitudinal health- and wellness-related datasets throughout the users' daily activities.

Results

Design principles of the freestanding electrochemical sensing system

Careful examination of the strain distribution of a typical microfluidic module, under motion-induced stress, yields near-zero strain at the bottom of the microfluidic channel (channel-biofluid interface). The resultant strain profile can be attributed to the absorption

and isolation of the strain by the load-bearing components of the microfluidic structure and biofluid, respectively. As shown in Fig. 1B, by recognizing and leveraging the fact that the strain-isolated region is the one that contains the sensor, we engineer a strain-isolated biomarker information delivery pathway that protects and routes the signal from the biofluid sensing interface all the way to the readout electronics.

To render an efficient pathway, we were inspired by integrin (*23, 24*), a cell adhesive molecule, which efficiently enables physiological information exchange between intracellular (*e.g.*, cytoskeleton) and extracellular matrices. As a single entity, integrin utilizes double-sided adhesion forces (*e.g.*, Van der Waals force) to facilitate sensing and out-of-plane signal interconnection (fig. S1, A). Accordingly, a generalizable and disposable freestanding electrochemical sensing system (FESS) is devised, which implements integrin-like functionalities through a strain-isolated region within a microfluidic structure (fig. S1, B).

The FESS is engineered as a vertically conductive, double-sided adhesive, and flexible microfluidic bioanalytical thin film system (fig. S2, 3). This thin film system consists of multiple vertically stacked films: an adhesive anisotropic conductive film (ACF), a noble metal electrode array film, a biochemical film, a microfluidic film (fig. S4, A to E, (*25, 26*)), and a skin adhesive film. The versatility of the FESS in terms of its core capabilities is demonstrated by depositing various patterns of different noble metals (gold Au and platinum Pt) as well as different sensing layers to target a panel of physiologically-relevant biomarker molecules in sweat. The inherent vertical conductivity of the FESS based on ACF allows for the realization of out-of-plane interconnection (Fig. 1C), which provides a degree of freedom for signal routing to avoid highly strained regions, thus preserving the transduced signal along the sensor-to-electronics signal pathway. The vertical conductivity and adhesive properties of the FESS, together, allow for direct interface with contact pads (fig. S4, F) on the readout electronics, eliminating the need for rigid connectors. Additionally, by including a microfluidic film, the thin film and inherently flexible system can be adapted for leakage-free epidermal biofluid (*e.g.*, sweat) harvesting and routing (fig. S4, G to K and fig. S5). The FESS can be adhered to skin and electronics, by leveraging its double-sided adhesive property.

As a complete thin film system, it can be simply taped onto the readout electronics without the need for any connectors, and with minimal contact resistance, thus potentially transforming any electrical contact into a chemo-/biosensor. The versatility of the FESS design allows for its implementation in various array formats (*e.g.*, 1 × 2, 3 × 3, 6 × 6, as exemplified in Fig. 1D to satisfy the end-application requirements. A representative self-contained biomarker sensing smartwatch, realized with the aid of FESS, is shown in Fig. 1E, which can monitor the sweat metabolite profiles of individuals in sedentary (Fig. 1F) and high intensity exercise settings (Fig. 1G).

A strain-isolated signal pathway

In this section, we first demonstrate the underlying physical phenomenon governing the superior performance of the out-of-plane (achieved by FESS) *vs.* conventional in-plane signal interconnection. Then, we characterize the out-of-plane electrical interconnection and mechanical adhesion properties of the FESS.

Conventional wearable microfluidic electrochemical sensors rely on in-plane signal interconnection (Fig. 2A) to relay the transduced signals to the readout circuitry. Therefore,

based on the implemented signal pathways, the signal is inevitably routed through body motion-induced strain-concentrated regions (including the 2D-patterned interconnects and/or the connector, fig. S6, A to C). Accordingly, they are severely susceptible to device operation failure (due to delamination, slipping, detachment, metal interconnect cracking, *etc*.) and interference (*e.g*., strain-induced noise), both of which lead to the loss of data fidelity.

In the implementation of the FESS, the inherent vertical conductivity of the ACF facilitates out-of-plane signal interconnection (Fig. 2A, similar to that shown in the reported advanced stretchable electronics (*27*)), which here, can be exploited as a degree of freedom for avoiding undesired body motion-induced strain effects on signal pathways. To illustrate this point, we simulated the strain profile experienced by a representative FESS (Fig. 2B), under an applied force (representing the force exerted along the skin-device interface due to the body motion). Figure 2C visualizes the corresponding strain distribution of a sensing pixel within the FESS, demonstrating that the maximal strain occurs in the regions where the microfluidic structure contacts with the substrate, while minimal strain occurs at the biofluid-substrate interface (encompassing the sensor). When constructing the signal pathway, the high strain regions can be avoided by leveraging the out-of-plane interconnection property of the FESS. As shown in Fig. 2D, this unique property of FESS allows for significantly reducing (by 2 orders of magnitude) the strain experienced by the transduced signals. This strain isolation strategy rendered by FESS can be generally adopted for interfacing electronics with different mechanical properties. Figure S6 (D) shows the simulated strain profiles for electronics with different substrate materials and Young's modulus (also detailed in table S1): stretchable PDMS (500 kPa), flexible polyimide board (2.5 GPa), and rigid board (24 GPa). In particular, the results shown in fig. S6 (D) indicate that the strain isolated regions are present in all scenarios (independent of the electronic substrate's stiffness). Additionally, the interconnection length rendered by FESS is ~50 μm (corresponding to the thickness of the ACF). This represents more than two orders of magnitude reduction in the transduced signal pathway, as compared to the conventional implementations with centimeter-scale interconnection routing, which is critical to the mitigation of external electromagnetic interference and mechanical noise.

We first establish the suitability of the ACF to simultaneously serve as an electrode supporting substrate and as an interconnection film. To pattern electrodes on ACF, the inherent adhesive property of the ACF was leveraged to directly deposit Au via e-beam metal evaporation. This approach eliminates the need for the metal adhesion layer (*e.g*., chromium or titanium), and subsequently allows for realizing a corrosion-resistant and stable interface for operation in biofluid environment (*28*).

To demonstrate the robustness of the out-of-plane signal interconnection against mechanical deformation, the FESS-based interconnection resistance distribution (R_{FESS}) of a representative 6 x 6 grid of Au ACF-based electrodes was characterized under spatially varying strain distribution profiles. Accordingly, the grid of electrodes was mated with a corresponding grid of flexible PCB-based contact pads (with resultant resistance distribution $R_{FESS} + R_{FPCB}$) via adhesion. Then, the resultant configuration was mounted on holders with localized tip radius curvature ($\alpha = 60°$, R = 15 mm and $\alpha = 30°$, R = 10 mm), such that the column 4 of the mated gird configuration experiences the maximal strain, while other columns experience minimal strain (conceptualized in Fig. 2E). By comparison of the R_{FESS} measurements of the 4th column with those of other columns, we can evaluate the effect of the stress concentration on the out-of-plane interconnection resistance across the

device. Our characterization results, shown in Fig. 2F, demonstrate that despite the high strain experienced by the 4th column (compared to the others), the corresponding out-of-plane interconnection resistances were minimally impacted across the device (for all three tested conditions, *i.e.*, flat, bent at 30°, and bent at 60°). The observed variations are on the order of 5%, which can be attributed to the error associated with the manual probing of the resistance values. The interconnection resistance (per unit area) levels for all cases are less than 0.025 Ω/mm^2, rendering less than 0.1 Ω of resistance, which is a fraction of the resistance contributed by the FPCB (Fig. 2G). This substantially low interconnection resistance can be attributed to the devised implementation of the interconnect, which realizes an effective cross-section resistor surface area A comparable to the size of the sensor (~ 1 mm × 1 mm as compared to conventional interconnects' cross section ~ 100 nm x 1 mm) and resistor length l of 50 µm (as compared to conventional interconnect lengths ~ 1 cm), representing orders of magnitude of reduction in resistance R, where $R \propto (l/A)$. Additional characterization results demonstrate minimal changes to the FESS-based interconnection (ACF) resistance, for different bending angles (fig. S7, A), upon performing cyclical bending and twisting (over 1000 cycles, respectively shown in fig. S7, B and C), and throughout different daily activities (fig. S7, D).

To characterize the mechanical adhesion property of the FESS, 180° peel adhesion tests were performed (as described in detail in the Methods section), because interfacial peeling properties are critical to the maintenance of robust interconnection between the FESS and electronics (*e.g.*, PCB). Specifically, the adhesion force between the FESS and electronics should be higher than that between the FESS and dry/actively sweat secreting skin (fig. S8, ~ 0.3 N/cm, in agreement with previously reported skin-adhesive medical tapes characterization results (*29, 30*)). Because the ACF layer in our devised thin film system bridges the FESS structure with electronics, we characterize the force required to peel the ACF layer of the FESS from a PCB. Given the influence of the backing structure (consisting of the microfluidic base and channel) on the peeling profile of the ACF, first, two test device structures were considered and characterized: one with double-sided tape backing (representing the microfluidic base) and one without (representing the microfluidic channel). The peeling forces corresponding to devices with/without backing were characterized as 10.3 N/cm and 2.7 N/cm, respectively (> 0.3 N/cm, Fig. 2, H and I). Following the same protocol, a representative FESS (as a complete device structure) containing periodic microfluidic features was also characterized. As shown in Fig. 2J, the measured peeling force profile illustrates a periodic pattern, tracing the interfacial features with and without the microfluidic structure backing, where the maximal and minimal peeling force levels correspond to the peeling forces of the two tested structures in Fig. 2H and Fig. 2I, respectively. For all characterized test device structures, the peeling forces were larger than 0.3 N/cm, indicating strong level of the FESS-based interconnection's adhesion to electronics, and validating its suitability for on-body applications.

Electrochemical signal transduction

In this section, we characterized the signal transduction capability of the FESS. Specifically, to achieve bio/chemical-to-electrical signal transduction, noble metal electrodes were patterned onto the ACF (forming the sensor substrate), followed by the deposition of designated bio/chemical films to target analytes of interest. We first characterized the electrochemical activity of the metal-patterned ACF for two commonly used electrode surfaces: unmodified Au and Pt nanoparticles (PtNP)-modified Au (which presents enhanced electrocatalytic performance in comparison to unmodified-Au (*31*)).

Next, cyclic voltammetry was used to test the electrochemical activity of the unmodified-Au and Au/PtNP patterned ACF in 0.1 M H_2SO_4 (Fig. 3A, B), in 0.1 M NaAc (pH = 7.2 – 7.8, fig. S9, A, B), and in 0.1 M NaOH (pH = 13.0, fig. S9, A, B) solutions (*32*). In Fig. 3A, hydrogen evolution reaction (HER) can be observed in the cathodic region, where the Au electrode inert potential window extends to ~ -0.1 V (*vs.* Ag/AgCl). In the anodic region, the adsorption of anions (*i.e.* OH^-, SO_4^{2-}) and of the initial gold surface oxidation occurs prior to oxygen evolution reaction (OER). The reduction peaks in this region are observed on reverse sweep, which arise from the gold oxide surface reduction and the desorption of ions. The same procedure was performed to characterize the PtNP-modified surface. As shown in Fig. 3B, the electrochemical characteristic of the PtNP-modified surface presents distinct signature peaks, which are related to hydrogen absorption/desorption of a Pt-based surface, indicating successful and stable PtNP modification of the electrode surface. Given the enhanced electrocatalytic activity of the PtNP-modified electrode in comparison to the unmodified Au electrode (fig. S9, C and D), the subsequent electrochemical biosensor development efforts were performed on the PtNP-modified electrode. This property can be exploited to detect electroactive species such as hydrogen peroxide (H_2O_2, sensitivity: 296.2 ± 20.0 μA/mM/cm^2 and limit of detection, LOD: 0.2 ± 0.06 μM, Fig. 3C), ascorbic acid, and dopamine with high sensitivity (fig. S9, E and F). In particular, the highly sensitive detection of H_2O_2 (the end-product of numerous enzymatic reactions) can be leveraged for targeting informative biomarkers (*e.g.*, glucose and lactate).The PtNP-modified electrode surface can be functionalized via the deposition of bio/chemical films to equip the FESS with chemo-/biosensing capability. Accordingly, the recognition elements of the film as well as the electrochemical interrogation method can be tailored to specifically target the biomarker molecules of interest. For example, Figure 3D-F show that enzymatic-based sensors can be combined with chronoamperometry to target glucose, lactate, and choline (the corresponding chemical composition of the sensing layer is shown in table S2). Additionally, iridium oxide-functionalized electrodes can be combined with open-circuit potential measurements to measure pH (fig. S9, G). These electroanalytical methods provide sample-to-answer biomarker readouts and are capable of rendering real-time insight into the alterations in the sweat bio-composition.

Here, we specifically adapted the sensing capability of the FESS to target glucose, lactate, and choline (all of which are present in non-invasive biofluids such as sweat (*33, 34*), as they are informative biomarkers of body metabolism and nutrition (*35, 36*)). The sensing interface for each target consists of an enzyme layer, coupled onto a poly-m-phenylenediamine (PPD)-layer, where the PPD layer serves as a permselective membrane to reject interfering species (*37, 38*). The response of each sensor toward the target analyte was first characterized individually. Figure 3D-F show the respective current responses of the glucose (sensitivity: 22.8 ± 0.7 μA/mM/cm^2 and LOD: 1.7 ± 0.7 μM), lactate (sensitivity: 4.1 ± 0.3 μA/mM/cm^2 and LOD: 4.6 ± 3.0 μM), and choline sensors (sensitivity: 9.4 ± 3.9 μA/mM/cm^2 and LOD: 10.5 ± 3.7 μM), measured amperometrically within their corresponding physiological relevant range (glucose: 0–1000 μM, lactate: 0–20 mM, choline: 0-350 μM, performed in phosphate-buffered saline, PBS). For all three sensors, the generated responses are proportional to the corresponding analyte's concentration levels. To ensure reliable operation in complex biofluids (here, sweat), the selectivity performances of the glucose and lactate sensors were characterized by measuring their responses towards a diverse panel of interfering species. As listed in Fig. 3G, the selected classes of interfering species include: electrolytes, electroactive species, drugs, sweat agonists, proteins, and other small molecules. As shown in Fig. 3H, I, both the glucose and lactate sensors exhibited negligible steady-state responses to the interfering species, while incremental addition of

the target analytes' concentration levels caused significant stepwise current responses. The sensing reliability of the FESS was further validated by performing a blind study, where a series of sample solutions were analyzed in random sequence by the FESS (taped onto contact pads) and a gold standard lab biochemistry analyzer (YSI 2900D). As shown in fig. S10 A and B, the biomarker levels measured by the corresponding sensors were very close to those measured by the lab instrument ($R^2_{Gluocse}$: 0.99 and $R^2_{Lactate}$: 0.95).

Furthermore, to demonstrate the multiplexed sensing capability of the FESS, the developed sensing interfaces were fabricated onto a single ACF, and the resultant functionalized film was taped onto a grid of PCB contact pads. The constructed sensor array's response was continuously monitored, while introducing different analytes at different timepoints. As shown in Fig. 3J, the sequential addition of 1 mM lactate, 100 μM choline, and 100 μM glucose correspondingly resulted in clear and stable stepwise response of the respective sensors. No crosstalk and corrosion-induced noise were observed during the multiplexed measurements. Moreover, amperometry (fig. S11, A to C) and open circuit potential (fig. S11, D and E) characterization experiments validated the electrochemical corrosion resistance of the FESS-PCB in saline solution environments, which is critical to ensure stable and extended sensing operation in biofluids and for the envisioned applications. Additional amperometry measurements performed under thermal cycling (25, 35 and 45°C) over an extended time period (> 1 hr) further demonstrated the operational stability of the FESS-PCB system (fig. S11, F). The FESS anti-corrosion lifetime is estimated to be at least 110 hrs at room temperature (as predicted by the performed accelerated life testing, fig. S11, G, and based on the Arrhenius model (*39*)).

FESS-enabled smartwatch for sweat biomarker monitoring during daily activities

To demonstrate the utility of the FESS for biomarker monitoring during the user's daily activities, the FESS was integrated with a custom-developed smartwatch as a model IoT device (Fig. 4A). The smartwatch hardware consists of analog/digital circuitries, a Bluetooth transceiver, and an LCD screen to implement system-level functionalities such as signal and user command processing, display, and wireless data communication (fig. S12, A to C). Depending on the user's needs, disposable FESS units with different sensing capabilities can be selected and taped onto the smartwatch by leveraging the reversibility of the adhesion forces of the FESS (fig. S12, D to H). The FESS-integrated smartwatch shows similar performance compared with those obtained by the potentiostat (fig. S12, I). An optional iontophoresis hardware module (a programmable current source), coupled with a ring-shaped pilocarpine-loaded hydrogel interface, is also implemented as a plugin unit for on-demand sweat induction in sedentary subjects (see more details in Method and fig. S12 J and K). The FESS-coupled and lithium polymer-powered hardware is embedded within a form-fitting 3D-printed casing. The complete smartwatch can be adhered onto the skin, without the need for any external wrapping or fixtures, to perform wireless biomarker sensing as a self-contained unit, and the obtained sensing data is linearly correlated with those obtained by a standard potentiostat. While the LCD screen displays the real-time readings and the temporal profile of the biomarker measurements, the Bluetooth transceiver module relays the readings to a custom-developed mobile application, which in turn uploads the data to a cloud-based server for further analysis.

To evaluate the signal stability of the FESS-enabled smartwatch against motion artifacts, a series of *ex-situ* and on-body experiments were performed to characterize the sensor response in the presence of varying motion characteristics in terms of frequency, orientation, acceleration, and externally applied contact force. For the *ex-situ* experiments, a FESS-

based glucose-sensor response was continuously recorded upon introduction of a blank and 100 μM glucose solutions (injected at 5 μL/min to mimic sweat secretion, into a microchannel with the height of 170 μm, containing a 2 mm × 3 mm glucose sensor), under stationary and three-dimensional oscillatory acceleration conditions (~10 m/s^2 at 5 Hz, generated by a vortical mixer). As shown in Fig. 4B and 4C, the measured sensor responses exhibit negligible fluctuations (< 6%) despite the induced motion, indicating the high fidelity of data achieved by the FESS-based system (similarly, as shown in Fig. S 13, stable responses were recorded for the microfluidic sensing modules with different channel heights and sensor dimensions, as well as the insufficient fluidic filling situation). Furthermore, for on-body characterization, a FESS-based lactate-sensor was integrated with the smartwatch worn by the subject, then the sensor's response to exercise-induced sweat was continuously recorded under various body motions, including punching, arm swinging, and forearm twisting, with varying acceleration, frequency, and orientation. Additionally, to quantify the effect of varying externally applied contact forces, different weights (1-2 N, similar force levels to that applied during finger tapping (*40*)) were applied to the smartwatch during the on-body lactate sensor response recordings. As shown in Fig. 4D-G, the measured sensor responses across all conditions exhibit negligible fluctuations (< 8%), indicating the suitability of the FESS-based smartwatch to render high fidelity biomarker data recording in presence of unconstrained body motion.

To demonstrate the utility of the wearable system for the envisioned diurnal and longitudinal biomarker monitoring, the FESS-enabled smartwatch was adhered on a subject's forearm, which was wirelessly controlled by the subject to take real-time sweat-based biomarker measurements at set time intervals in relation to the user's daily routine. The smartwatch was used by the subject to monitor his iontophoretically-induced sweat glucose levels before/after the consumption of mixed meals (*e.g.*, at the user's routine lunch and dinner times). As illustrated in Fig. 4H, I, the smartwatch glucose sensor readouts indicate the elevation of the subject's sweat glucose level upon food intake, which is in line with previously reported trends (*41*). Additionally, the smartwatch was used by the subject to monitor the sweat lactate profile (Fig. 4J) during running in a field. The smartwatch readouts indicated stable sweat lactate readings, despite the presence of relatively high frequency and high acceleration body motions involved in the running session.

Discussion

Here, by examining the biomarker information delivery pathway and recognizing near-zero strained regions within a microfluidic-based sensing module, we engineered a strain-isolated pathway to preserve the biomarker data fidelity. To render an efficient implementation, inspired by integrin (a cell adhesive molecule), which facilitates physiological information exchange between biological interfaces via sensing, out-of-plane signal interconnection, and double-sided adhesion forces, a generalizable and disposable electrochemical thin film sensing system is devised. The thin film system renders integrin-like functionalities in terms of signal transduction and co-axial signal interconnection/double-sided adhesion forces, all within a freestanding entity (namely, FESS). The FESS can reliably bridge the skin and the readout electronics to harvest biomarker information. The FESS also serves as a foundation to realize an unprecedented system-level design strategy to simultaneously address the challenges of wearable biosensing and integration with consumer electronics for daily use. To illustrate this objective, the FESS is seamlessly coupled with a custom-developed smartwatch. The robustness of the FESS-enabled smartwatch was validated by monitoring the real-time biomarker readouts throughout the user's daily routine activities. The versatility of the FESS

can be exploited to target a wide panel of biomarkers. The design methodology can be equivalently adopted to construct physical sensing interfaces in order to characterize the informative metrics related to the sweat secretion profile (*e.g.*, the onset of sweating, secretion rate, and sweat loss volume). The inclusion of such interfaces can be particularly useful for devising correction mechanisms toward mitigating the confounding effect of inter/intra-subject physiological variations and gland activity variability (in terms of metabolism and secretion rate), which have been reported to distort the physiological significance of the raw sweat readings (*42-46*).

Ultimately, to commercialize and adapt the presented wearable technology for population-level health and wellness monitoring, future clinical trials are required to map the sweat-based biomarker readings to the physiological status of the users, while accounting for the biological factors such as inter/intra individual and anatomical variations. In that regard, the advantages of our technology in terms of its ease of integration with wearable consumer electronics and its ability to generate of high-fidelity biomarker readings can be particularly harnessed to perform large-scale and longitudinal clinical investigations. The large data sets rendered by such studies enables the physiological-meaningful interpretation of the biomarker readings and the establishment of the objective criteria necessary to provide actionable feedback to the users.

Materials and Methods

Fabrication Process of the FESS

The FESS, a thin film system, consists of multiple vertically stacked films: (1) a double-sided adhesive anisotropic conductive film (9703, 3M, 50 μm, ACF), (2) a noble metal electrode array patterned on ACF, (3) a bioanalytical film deposited on the electrodes as a sensing interface, (4) a thin-film microfluidic structure which houses biosensors, and (5) a double-sided skin adhesive film which facilitates the adherence of the FESS's microfluidic module to the skin. The fabrication process of the FESS is as follows:

1. **Electrode array patterning and characterization on ACF:** First, an ACF was used as the substrate for electrode array patterning. One of the adhesive surfaces was covered with a pre-patterned mask for metal deposition. A 200 nm thick Au layer was thermally deposited onto the ACF to create an Au electrode array. For the Pt-based electrode array, platinum nanoparticles (PtNP) were deposited onto the Au electrodes by chemical reduction in an aqueous solution of 2.5 mM H_2PtCl_6 and 1.5 mM formic acid (-0.1 V *vs.* Ag/AgCl, 10 min) to construct the PtNP-coated Au electrodes (Au/PtNP) (*47*). Cyclic voltammetry was used to examine their cathodic and anodic currents (under a three-electrode system) using a potentiostat (CHI660E, CH instrument, USA). The experiments were performed in fresh 0.1 M H_2SO_4 solution/0.1 M NaAc/0.1 M NaOH solution and the potential was scanned at a rate of 25 mV/s.

2. **Biosensing interface construction:** A poly-m-phenylenediamine (PPD) layer was electrochemically deposited onto the Au/PtNP electrodes by applying 0.85 V (*vs.* Ag/AgCl) for 300 s in a fresh PBS solution (Gibco® PBS, ThermoFisher, pH 7.2) with 5 mM m-phenylenediamine (Sigma-Aldrich). Then, the Au/PtNP/PPD electrodes were washed with deionized (DI) water and air-dried. Next, the electrode array was transferred to a low adhesion release paper liner (72#, 3M) by using PVA water-soluble tape (5414, 3M) and rinsed in DI water to remove residual particles. A 1% chitosan solution (Sigma-Aldrich) was prepared by dissolving chitosan in a

2% acetic acid (Sigma-Aldrich) solution by heating it up to 60 °C for 30 min until chitosan was fully dissolved. To develop the glucose sensor, the aforementioned 1% chitosan solution was mixed thoroughly with a glucose oxidase solution (Sigma-Aldrich, 50 mg/mL in PBS, pH 7.2) at a ratio of 1:1 (volume/volume). By drop casting 1 µL of the mixture onto the Au/PtNP/PPD electrode (12 mm^2), the glucose sensing interface was realized. To create the choline sensor, a 0.5 µL choline oxidase solution (Sigma-Aldrich, 0.5 unit/µL in DI water, pH 7.2) was placed onto the Au/Pt/PPD electrode (12 mm^2), dried at room temperature, and was followed by drop casting a 0.5 µL 1% chitosan solution. To create the lactate sensor, a 4 µL Lactate oxidase solution (Toyobo, 50 mg/mL in PBS) was deposited onto Au/PtNP/PPD electrode (12 mm^2) and dried at room temperature, followed by drop casting of a 2 µL 1% Chitosan solution and a 2 µL 3% polyvinyl chloride (PVC, Sigma-Aldrich) solution (*48*). The sensors were allowed to dry overnight at 4 °C, while being protected from light. They were stored at 4 °C when not in use. For pH sensor, iridium oxide (IrOx) was electrodeposited following previously reported protocols (*49, 50*). For all biosensors, the reference electrode was fabricated by depositing Ag/AgCl ink (Ercon) on the electrodes and heating the modified electrodes at 80 °C for 10 min. The Au/PtNP electrode was used as the counter electrode.

3. **Microfluidic module assembly:** Microfluidic channels were created by laser-cutting (Epilog Mini 24, Epilog Laser) 2D patterns on the double-sided tape (~170 µm). By laser patterning holes on PET (MG Chemicals, ~100 µm), outlet features were created to facilitate an ejection path for the sampled biofluid. The microfluidic structure/module was then assembled by attaching the patterned PET layer to the patterned double-sided tape with proper alignment, such that the filling of the microfluidic channel results in the coverage of the working electrode first, and then the reference electrode. In this way, it is ensured that the working electrode with pre-defined surface area is fully covered when the electrical signal appears upon the establishment of the fluid connection between the two electrodes. The microfluidic structure served as the strain-isolated housing for all biosensors (constructed on ACF).

Finite element analysis (FEA) and mechanical modeling of the FESS

FEA software, COMSOL 5.2, was used to simulate the mechanical behavior of the FESS under the directional shear load expected during usage. A 3D model of the FESS, mounted on the readout electronics, was used for the mechanical analysis with no delamination between layers being considered. In-plane directional shear force was applied on the skin adhesive layer with the base of electronics fixed. Similarly, the strain profile of the conventional in-plane interconnection subjected to a directional shear load and a bi-directional stretch load was analyzed using a 2D demo structure. For directional shearing, 10% displacement along the skin surface was applied on the µ-fluidics structure interfacing the skin and the displacement of the readout electronics was set to zero. For bi-directional stretching, displacements corresponding to 10% skin stretching were applied on both the readout electronics and the µ-fluidics interfacing the skin. The strain distributions and magnitudes were captured for each simulation. The Young's modulus and Poisson's ratio used in the simulations were: 450 MPa and 0.49 for the ACF, skin adhesive and µ-fluidics structure; 2.5 GPa and 0.4 for PET; 24 GPa and 0.12 for the rigid electronics (FR-4); 2.5 GPa and 0.4 for flexible electronics (PI); 500 kPa and 0.49 for stretchable electronics (PDMS).

Contact resistance measurement of the FESS

The electrical resistance between the ENIG (electroless nickel/Immersion gold) contact pads (6 × 6 array, on a FPCB) and their corresponding pins were measured and recorded by a multimeter (Fluke-299), as initial resistances. Then, an ACF layer patterned with corresponding 6 × 6 Au electrode array was transferred onto the ENIG contact pads with proper alignment. The ACF-FPCB was mounted onto the curved surface of 3D-printed holder. The resistance for each pixel of the Au array on ACF was measured again by the same multimeter. Each resistance value was determined by averaging measured resistances from three different positions of the electrode surface.

Peel adhesion test of the FESS

The peel adhesion force (interfacial toughness) between the FESS and the PCB was determined by performing standard 180°-peeling tests, based on ASTM D3330, with a mechanical testing machine (Instron 5943). At first, the ACF, microfluidic-channel-patterned double-sided tape, and PET were laser-cut and assembled into 30 mm wide and 300 mm long strips. The patterned double-sided tape and PET served as the microfluidic structure, which can be considered as the backing material for the ACF. During the test, the ACF side of the laminated FESS strip was thumb-pressed onto the PCB to ensure a uniform and tight bond. The samples were prepared in less than 1 day prior to the mechanical tests. The peeling tests were performed with the standard 180°-peeling method at a speed of 5 mm/s in ambient air at room temperature. The force *vs.* displacement profile was directly output by the Instron, and the peeling adhesion force/interfacial toughness was calculated by dividing the measured peeling force by the sample width.

Biosensor characterization and analytes measurement

To characterize the developed enzymatic sensing interfaces, constant potential amperometric measurements were conducted in PBS buffer (pH = 7.2) at + 0.5 V *vs.* Ag/AgCl. The amperometric response was continuously recorded by a potentiostat under constant stirring. By stepwise addition of different concentrations of the target analytes (*e.g.*, glucose, lactate, and choline) in the PBS buffer for different sensors, a series of calibration plots were obtained. The limit of detection (LOD) for each amperometric sensing interface was calculated as LOD = 3*SD/(slope of calibration curve), where SD is the standard deviation of the baseline noise in blank solution. To characterize the IrOx pH sensor, open circuit potential (OCP) was measured against a separate Ag/AgCl reference. The PBS was titrated with NaOH/HCl to vary the pH from 4.1 to 10.15 and each stabilized OCP was recorded. The sensor selectivity tests were performed by the stepwise addition of different interferents into PBS, including glucose/lactate, creatine, KCl, NaCl, UA, AA, Pilocarpine, Aspirin, Metformin, and Albumin. At the end of the selectivity test, the target analytes were also added into the solutions.

Anti-corrosion capability of the FESS-PCB

Two PCBs with ENIG-based electrodes (18 mm^2) and a Pt disk electrode (1.6 mm in diameter) were cleaned with DI water and IPA solution, then dried in air at room temperature. The ACF with Au/PtNP was transferred and aligned with the electrodes on one PCB and the other PCB was left unmodified as a control. The unmodified PCB, PCB with Au/PtNP patterned ACF, and Pt disk electrode were immersed into a PBS solution followed by OCP and corrosion current measurements. For OCP measurement, the voltage was recorded using a potentiostat. For corrosion current measurement, + 0.5 V (*vs.* Ag/AgCl) was applied under constant stirring.

Ex-situ signal fidelity characterization of the FESS-PCB

The FESS-PCB system and an accelerometer (mobile phone) were fixed onto a vortex mixer (Fisher Scientific). The blank PBS and PBS containing 100 μM glucose were sequentially injected into the FESS with a controlled flow rate (5 μL/min). The electrochemical signal was then recorded by a potentiostat during stationary and motion-induced (via vortex mixer, frequency = 5 Hz) conditions.

On-body test using the FESS-integrated smartwatch

The FESS was transferred onto the contact pads located on the backside of the custom-developed smartwatch. Then, the FESS-coupled smartwatch was adhered onto a healthy human subject's wrist. A smartwatch case was designed and 3D-printed to consolidate the smartwatch components (including LCD display, PCB module, and battery). In addition to the smartwatch, a mobile phone (equipped with an accelerometer) was mounted onto the subject's forearm to record the acceleration of his forearm during the exercise. To induce sweat iontophoretically, the target stimulation area of the skin was first cleaned with DI water and ethanol, followed by 5 minutes of iontophoretic sweat gland stimulation (with pilocarpine-loaded hydrogels, Pilogel).

Wireless PCB module

The wireless PCB module implements the required sweat stimulation circuitries to drive the iontophoresis electrode, as well as signal conditioning and processing circuitries to reliably measure the transduced sensing signals. The electrical connections from the iontophoresis/sensing layers with the main board were established by the metal vias, embedded within each layer. At its core, the PCB utilized an ultra-low-power microcontroller unit (STM8L – UFQFN20, STMicroelectronics), which was programmed to facilitate system level functionalities. These functionalities include setting the current levels for iontophoresis (accompanied with a current limiting protection circuitry) and providing I2C-controlled signals for the sensing and serial data communication modules. The microcontroller is interfaced with an onboard Bluetooth transceiver to wirelessly and bilaterally communicate the command and sensor output data with a custom-developed smartphone application. Moreover, the microcontroller communicates with an onboard LCD screen (st7735 – TFT-LCD, Sitronix Technology Corporation) to display the biomarker readouts, iontophoresis current level, and the local time.

An analog signal acquisition and conditioning circuitry was developed to interface the amperometric sensors and process the transduced signals. Accordingly, after the sensing mode is activated, an LMP91000 potentiostat chip (Texas Instruments) was enabled. This chip was programmed to maintain +0.5 V across the working and reference electrodes, and to convert the transduced sensor current to voltage values by leveraging its internal transimpedance amplifier stage. The output of the potentiostat was connected to a fifth-order low-pass filter (LPF), which was realized by a MAX7422 chip (Maxim Integrated), with a cut-off frequency of 1 Hz. The LPF stage mitigates the high frequency interference and the user's motion artifacts. The microcontroller's built-in 12-bit Analog-to-Digital (ADC) unit was used to convert the LPF's analog output to the digital domain. The measured amperometric sensor response by the PCB was validated against a potentiostat.

In our PCB development efforts, we selected integrated circuit chips that were designed for low-power/ultra-low-power applications to implement a power efficient system. To power the PCB, a single miniaturized rechargeable lithium-ion polymer battery with a nominal voltage of 3.7 V was used. The choice for the battery's capacity depends on the intended

modes and duration of operations. Based on our characterization results, with no further power optimization, the envisioned simultaneous operations (*e.g.*, iontophoresis, sensing, and bilateral wireless communication) demanded peak supply current levels on the order of 100 mA. For an application such as periodic sweat sampling and analysis at 6 points during the day (*e.g.*, monitoring glucose levels before/after main meals), and assuming 15 minutes of active operation, a battery capacity on the order of 500 mAh would be sufficient.

Smartphone application and smartwatch design

To wirelessly communicate with the PCB module from the user standpoint, an Android-based smartphone application was developed. The application provides a graphical user interface to execute a range of functionalities, including setting the desired operational modes as well as data display and storage. In our implementation, the user input is read and relayed to the PCB through Bluetooth communication of predefined integer values (each value mapped to a desired operation). Then, the corresponding command is received and executed at the microcontroller level.

The custom smartphone application design/cloud server

The Android application is designed to establish communication with the paired/specified custom-developed smartwatch upon startup. Once the communication is established, the user has the option to program the desired iontophoresis current level for sweat stimulation. Additionally, the user can switch between the iontophoresis and sensing modes with the press of a button. In sensing mode, the real-time and filtered sensing results are recorded, timestamped, and plotted by the application. Finally, the sweat metabolite data captured by the application are automatically stored on a custom-developed Google Cloud platform.

Institutional Review Board (IRB) approval for human subject testing

The conducted human subject experiments were performed in compliance with the protocols approved by the IRB at the University of California, Los Angeles (IRB#17-000170). All subjects gave written informed consent before participation in the study.

Supplementary Materials

Fig. S1. Bio-inspired *in-situ* sensing and signal interconnection.
Fig. S2. Design and fabrication of FESS components.
Fig. S3. Liner exchange procedure for the FESS construction.
Fig. S4. Visualization of the microfluidic module of the FESS and its integration with skin and electronics.
Fig. S5. Visualization of the FESS-skin reliable adhesion.
Fig. S6. Mechanical strain simulation of different implementations.
Fig. S7. The effect of mechanical deformation on the FESS electrical interconnection (ACF) resistance.
Fig. S8. Skin adhesive peeling test.
Fig. S9. Electrochemical properties of Au and Au/PtNP electrode surface of the FESS.
Fig. S10. FESS-based electrochemical sensor accuracy validation.
Fig. S11. Anti-corrosion property of the FESS in aqueous environment.
Fig. S12. FESS-enabled smartwatch.
Fig. S13. *Ex-situ* characterization of the signal stability of FESS-PCB glucose sensing system in presence of vortical vibration.
Table S1. Structural composition of FESS.
Table S2. Chemical composition of FESS sensing interface.
Movie S1. ACF-based interconnection under mechanical deformation.

References and Notes

1 R. Byrne, D. Diamond. Chemo/bio-sensor networks. *Nat. Mater.* **5**, 421-424 (2006).

2 B. Farahani, F. Firouzi, V. Chang, M. Badaroglu, N. Constant, K. Mankodiya. Towards fog-driven IoT eHealth: Promises and challenges of IoT in medicine and healthcare. *Future Gener. Comp. Sy.* **78**, 659-676 (2018).

3 H. U. Chung, B. H. Kim, J. Y. Lee, J. Lee, Z. Q. Xie, E. M. Ibler, K. Lee, A. Banks, J. Y. Jeong, J. Kim, C. Ogle, D. Grande, Y. Yu, H. Jang, P. Assem, D. Ryu, J. W. Kwak, M. Namkoong, J. B. Park, Y. Lee, D. H. Kim, A. Ryu, J. Jeong, K. You, B. W. Ji, Z. J. Liu, Q. Z. Huo, X. Feng, Y. J. Deng, Y. S. Xu, K. I. Jang, Y. H. Zhang, R. Ghaffari, C. M. Rand, M. Schau, A. Hamvas, D. E. Weese-Mayer, Y. G. Huang, S. M. Lee, C. H. Lee, N. R. Shanbhag, A. S. Paller, S. Xu, J. A. Rogers. Binodal, wireless epidermal electronic systems with in-sensor analytics for neonatal intensive care. *Science* **363**, eaau0780 (2019).

4 Y. Khan, M. Garg, Q. Gui, M. Schadt, A. Gaikwad, D. G. Han, N. A. D. Yamamoto, P. Hart, R. Welte, W. Wilson, S. Czarnecki, M. Poliks, Z. P. Jin, K. Ghose, F. Egitto, J. Turner, A. C. Arias. Flexible Hybrid Electronics: Direct Interfacing of Soft and Hard Electronics for Wearable Health Monitoring. *Adv. Funct. Mater.* **26**, 8764-8775 (2016).

5 C. H. Wang, X. S. Li, H. J. Hu, L. Zhang, Z. L. Huang, M. Y. Lin, Z. R. Zhang, Z. N. Yin, B. Huang, H. Gong, S. Bhaskaran, Y. Gu, M. Makihata, Y. X. Guo, Y. S. Lei, Y. M. Chen, C. F. Wang, Y. Li, T. J. Zhang, Z. Y. Chen, A. P. Pisano, L. F. Zhang, Q. F. Zhou, S. Xu. Monitoring of the central blood pressure waveform via a conformal ultrasonic device. *Nat. Biomed. Eng.* **2**, 687-695 (2018).

6 C. M. Boutry, Y. Kaizawa, B. C. Schroeder, A. Chortos, A. Legrand, Z. Wang, J. Chang, P. Fox, Z. N. Bao. A stretchable and biodegradable strain and pressure sensor for orthopaedic application. *Nat. Electron.* **1**, 314-321 (2018).

7 C. Wang, D. Hwang, Z. B. Yu, K. Takei, J. Park, T. Chen, B. W. Ma, A. Javey. User-interactive electronic skin for instantaneous pressure visualization. *Nat. Mater.* **12**, 899-904 (2013).

8 S. Emaminejad, W. Gao, E. Wu, Z. A. Davies, H. Y. Y. Nyein, S. Challa, S. P. Ryan, H. M. Fahad, K. Chen, Z. Shahpar, S. Talebi, C. Milla, A. Javey, R. W. Davis. Autonomous sweat extraction and analysis applied to cystic fibrosis and glucose monitoring using a fully integrated wearable platform. *Proc. Natl. Acad. Sci. USA* **114**, 4625-4630 (2017).

9 A. Hauke, P. Simmers, Y. R. Ojha, B. D. Cameron, R. Ballweg, T. Zhang, N. Twine, M. Brothers, E. Gomez, J. Heikenfeld. Complete validation of a continuous and blood-correlated sweat biosensing device with integrated sweat stimulation. *Lab Chip* **18**, 3750-3759 (2018).

10 W. Gao, S. Emaminejad, H. Y. Y. Nyein, S. Challa, K. V. Chen, A. Peck, H. M. Fahad, H. Ota, H. Shiraki, D. Kiriya, D. H. Lien, G. A. Brooks, R. W. Davis, A. Javey. Fully integrated wearable sensor arrays for multiplexed in situ perspiration analysis. *Nature* **529**, 509-514 (2016).

11 A. Koh, D. Kang, Y. Xue, S. Lee, R. M. Pielak, J. Kim, T. Hwang, S. Min, A. Banks, P. Bastien, M. C. Manco, L. Wang, K. R. Ammann, K. I. Jang, P. Won, S. Han, R. Ghaffari, U. Paik, M. J. Slepian, G. Balooch, Y. G. Huang, J. A. Rogers. A soft, wearable microfluidic device for the capture, storage, and colorimetric sensing of sweat. *Sci. Transl. Med.* **8**, 366ra165 (2016).

12 S. Imani, A. J. Bandodkar, A. M. V. Mohan, R. Kumar, S. F. Yu, J. Wang, P. P. Mercier. A wearable chemical-electrophysiological hybrid biosensing system for real-time health and fitness monitoring. *Nat. Commun.* **7**, 11650 (2016).

13 H. Lee, C. Song, Y. S. Hong, M. S. Kim, H. R. Cho, T. Kang, K. Shin, S. H. Choi, T. Hyeon, D. H. Kim. Wearable/disposable sweat-based glucose monitoring device with multistage transdermal drug delivery module. *Sci. Adv.* **3**, e1601314 (2017).

14 Y. J. Hong, H. Lee, J. Kim, M. Lee, H. J. Choi, T. Hyeon, D. H. Kim. Multifunctional Wearable System that Integrates Sweat-Based Sensing and Vital-Sign Monitoring to Estimate Pre-/Post-Exercise Glucose Levels. *Adv. Funct. Mater.* **28**, 1805754 (2018).

15 H. Y. Y. Nyein, L. C. Tai, Q. P. Ngo, M. H. Chao, G. B. Zhang, W. Gao, M. Bariya, J. Bullock, H. Kim, H. M. Fahad, A. Javey. A Wearable Microfluidic Sensing Patch for Dynamic Sweat Secretion Analysis. *ACS Sens.* **3**, 944-952 (2018).

16 Y. H. Zhang, S. D. Wang, X. T. Li, J. A. Fan, S. Xu, Y. M. Song, K. J. Choi, W. H. Yeo, W. Lee, S. N. Nazaar, B. W. Lu, L. Yin, K. C. Hwang, J. A. Rogers, Y. G. Huang. Experimental and Theoretical Studies of Serpentine Microstructures Bonded To Prestrained Elastomers for Stretchable Electronics. *Adv. Funct. Mater.* **24**, 2028-2037 (2014).

17 K. D. Harris, A. L. Elias, H. J. Chung. Flexible electronics under strain: a review of mechanical characterization and durability enhancement strategies. *J. Mater. Sci.* **51**, 2771-2805 (2016).

18 M. Bariya, H. Y. Y. Nyein, A. Javey. Wearable sweat sensors. *Nat. Electron.* **1**, 160-171 (2018).

19 M. Gonzalez, F. Axisa, M. V. Bulcke, D. Brosteaux, B. Vandevelde, J. Vanfleteren. Design of metal interconnects for stretchable electronic circuits. *Microelectron. Reliab.* **48**, 825-832 (2008).

20 J. Cai, K. Cizek, B. Long, K. McAferty, C. G. Campbell, D. R. Allee, B. D. Vogt, J. La Belle, J. Wang. Flexible thick-film electrochemical sensors: Impact of mechanical bending and stress on the electrochemical behavior. *Sensor Actuat. B-chem* **137**, 379-385 (2009).

21 A. Romeo, Q. H. Liu, Z. G. Suo, S. P. Lacour. Elastomeric substrates with embedded stiff platforms for stretchable electronics. *Appl. Phys. Lett.* **102** (2013).

22 Y. J. Ma, M. Pharr, L. Wang, J. Kim, Y. H. Liu, Y. G. Xue, R. Ning, X. F. Wang, H. U. Chung, X. Feng, J. A. Rogers, Y. Huang. Soft Elastomers with Ionic Liquid-Filled Cavities as Strain Isolating Substrates for Wearable Electronics. *Small* **13**, 1602954 (2017).

23 M. J. Dalby, N. Gadegaard, R. O. C. Oreffo. Harnessing nanotopography and integrin-matrix interactions to influence stem cell fate. *Nat. Mater.* **13**, 558-569 (2014).

24 C. K. Miranti, J. S. Brugge. Sensing the environment: a historical perspective on integrin signal transduction. *Nat. Cell Biol.* **4**, E83-E90 (2002).

25 H. S. Lin, Y. C. Zhao, S. Y. Lin, B. Wang, C. Yeung, X. B. Cheng, Z. Q. Wang, T. Y. Cai, W. Z. Yu, K. King, J. W. Tan, K. Salahi, H. Hojaiji, S. Emaminejad. A rapid and low-cost fabrication and integration scheme to render 3D microfluidic architectures for wearable biofluid sampling, manipulation, and sensing. *Lab Chip* **19**, 2844-2853 (2019).

26 H. S. Lin, H. Hojaiji, S. Y. Lin, C. Yeung, Y. C. Zhao, B. Wang, M. Malige, Y. B. Wang, K. King, W. Z. Yu, J. W. Tan, Z. Q. Wang, X. B. Cheng, S. Emaminejad. A wearable electrofluidic actuation system. *Lab Chip* **19**, 2966-2972 (2019).

27 Z. L. Huang, Y. F. Hao, Y. Li, H. J. Hu, C. H. Wang, A. Nomoto, T. S. Pan, Y. Gu, Y. M. Chen, T. J. Zhang, W. X. Li, Y. S. Lei, N. Kim, C. F. Wang, L. Zhang, J. W. Ward, A. Maralani, X. S. Li, M. F. Durstock, A. Pisano, Y. Lin, S. Xu. Three-dimensional integrated stretchable electronics. *Nat. Electron.* **1**, 473-480 (2018).

28 L. L. Qiang, S. Vaddiraju, J. F. Rusling, F. Papadimitrakopoulos. Highly sensitive and reusable Pt-black microfluidic electrodes for long-term electrochemical sensing. *Biosens. Bioelectron.* **26**, 682-688 (2010).

29 J. Kim, Y. Hwang, S. Jeong, S. Y. Lee, Y. Choi, S. Jung. An elastomer for epidermal electronics with adjustable adhesion force and stretchability obtained via a reverse-micelle-induced process. *J. Mater. Chem. C* **6**, 2210-2215 (2018).

30 L. Liu, K. Kuffel, D. K. Scott, G. Constantinescu, H. J. Chung, J. Rieger. Silicone-based adhesives for long-term skin application: cleaning protocols and their effect on peel strength. *Biomed. Phys. Eng. Express* **4**, 015004 (2018).

31 X. Li, D. Heryadi, A. A. Gewirth. Electroreduction activity of hydrogen peroxide on Pt and Au electrodes. *Langmuir.* **21**, 9251-9259 (2005).

32 J. D. Benck, B. A. Pinaud, Y. Gorlin, T. F. Jaramillo. Substrate Selection for Fundamental Studies of Electrocatalysts and Photoelectrodes: Inert Potential Windows in Acidic, Neutral, and Basic Electrolyte. *Plos One* **9**, e107942 (2014).

33 V. P. Kutyshenko, M. Molchanov, P. Beskaravayny, V. N. Uversky, M. A. Timchenko. Analyzing and Mapping Sweat Metabolomics by High-Resolution NMR Spectroscopy. *Plos One* **6**, e28824 (2011).

34 S. S. Craig, S. A. S. Craig, M. S. Ganio, C. M. Maresh, H. Greg, K. A. da Costa, S. H. Zeisel. The betaine content of sweat from adolescent females. *J. Int. Soc. Sports Nutr.* **7**, 3 (2010).

35 J. Moyer, D. Wilson, I. Finkelshtein, B. Wong, R. Potts. Correlation Between Sweat Glucose and Blood Glucose in Subjects with Diabetes. *Diabetes Technol. Ther.* **14**, 398-402 (2012).

36 Z. Sonner, E. Wilder, J. Heikenfeld, G. Kasting, F. Beyette, D. Swaile, F. Sherman, J. Joyce, J. Hagen, N. Kelley-Loughnane, R. Naik. The microfluidics of the eccrine sweat gland, including biomarker partitioning, transport, and biosensing implications. *Biomicrofluidics* **9**, 031301 (2015).

37 X. Wen, B. Wang, S. Huang, T. Liu, M. S. Lee, P. S. Chung, Y. T. Chow, L. W. Huang, H. G. Monbouquette, N. T. Maidment, P. Y. Chiou. Flexible, multifunctional neural probe with liquid metal enabled, ultra-large tunable stiffness for deep-brain chemical sensing and agent delivery. *Biosens. Bioelectron.* **131**, 37-45 (2019).

38 B. Wang, B. Koo, L. W. Huang, H. G. Monbouquette. Microbiosensor fabrication by polydimethylsiloxane stamping for combined sensing of glucose and choline. *Analyst.* **143**, 5008-5013 (2018).

39 L. A. Escobar, W. Q. Meeker. A review of accelerated test models. *Stat. Sci.* **21**, 552-577 (2006).

40 D. S. Asakawa, G. H. Crocker, A. Schmaltz, D. L. Jindrich. Fingertip forces and completion time for index finger and thumb touchscreen gestures. *J. Electromyogr. Kinesiol.* **34**, 6-13 (2017).

41 A. J. Bandodkar, W. Z. Jia, C. Yardimci, X. Wang, J. Ramirez, J. Wang. Tattoo-Based Noninvasive Glucose Monitoring: A Proof-of-Concept Study. *Anal. Chem.* **87**, 394-398 (2015).

42. J. Moyer, D. Wilson, I. Finkelshtein, B. Wong, R. Potts. Correlation Between Sweat Glucose and Blood Glucose in Subjects with Diabetes. *Diabetes Technol. Ther.* **14**, 398-402 (2012).

43. A. Jajack, M. Brothers, G. Kasting, J. Heikenfeld. Enhancing glucose flux into sweat by increasing paracellular permeability of the sweat gland. *Plos One* **13**, e0200009 (2018).

44. Z. Sonner, E. Wilder, J. Heikenfeld, G. Kasting, F. Beyette, D. Swaile, F. Sherman, J. Joyce, J. Hagen, N. Kelley-Loughnane, R. Naik. The microfluidics of the eccrine sweat gland, including biomarker partitioning, transport, and biosensing implications. *Biomicrofluidics* **9**, 031301 (2015).
45. J. Heikenfeld, A. Jajack, B. Feldman, S. W. Granger, S. Gaitonde, G. Begtrup, B. A. Katchman. Accessing analytes in biofluids for peripheral biochemical monitoring. *Nat. Biotechnol*. **37**, 407-419 (2019).
46. M. J. Buono, N. V. L. Lee, P. W. Miller. The relationship between exercise intensity and the sweat lactate excretion rate. *J. Physiol. Sci*. **60**, 103-107 (2010).
47 C. Boehler, T. Stieglitz, M. Asplund. Nanostructured platinum grass enables superior impedance reduction for neural microelectrodes. *Biomaterials*. **67**, 346-353 (2015).
48 A. J. Bandodkar, P. Gutruf, J. Choi, K. Lee, Y. Sekine, J. T. Reeder, W. J. Jeang, A. J. Aranyosi, S. P. Lee, J. B. Model, R. Ghaffari, C. J. Su, J. P. Leshock, T. Ray, A. Verrillo, K. Thomas, V. Krishnamurthi, S. Han, J. Kim, S. Krishnan, T. Hang, J. A. Rogers. Battery-free, skin-interfaced microfluidic/electronic systems for simultaneous electrochemical, colorimetric, and volumetric analysis of sweat. *Sci. Adv.* **5**, eaav3294 (2019).
49 K. Yamanaka. Anodically Electrodeposited Iridium Oxide Films (AEIROF) from Alkaline Solutions for Electrochromic Display Devices. *Jpn. J. Appl. Phys.* **28**, 632-637 (1989).
50 V. M. Tolosa, K. M. Wassum, N. T. Maidment, H. G. Monbouquette. Electrochemically deposited iridium oxide reference electrode integrated with an electroenzymatic glutamate sensor on a multielectrode array microprobe. *Biosens. Bioelectron.* **42**, 256-260 (2013).

Acknowledgments

The authors appreciate the members of the Center for Minimally Invasive Therapeutics (C-MIT), UCLA nanoelectronics research facility (NRF), and Lux Lab (Doug Daniels) for their help in device fabrication/characterization and instrumentation sharing. The authors extend their gratitude to Professors Patricia A. Deuster, Hanlee P. Ji, Alan Grinnell and Karen Lyons and Dr. Lincoln Nadauld for providing feedback on the presented work and insightful discussions. The authors also thank Andy Vo, Jonghwee Park, Arjun Bodduand, and Shuxin Tan for their assistance with device fabrication and circuit design, as well as Amir Mohammad Hojaiji and Ruikun Li for 3D concept figure design.

Funding: This work was supported by the S.E.'s startup package provided by the UCLA Henry Samueli School of Engineering and Applied Sciences. Components of research are supported by the National Science Foundation (Award #1847729), Henry M. Jackson Foundation, Stanford Genome Technology Center Distinguished Young Investigator Award (in partnership with Intermountain Healthcare), Brain and Behavior Foundation (NARSAD Young Investigator Grant), and PhRMA Foundation (Research Starter Grant in Translational Medicine and Therapeutics).

Author contributions: Y.Z., B.W. and S.E. conceived the idea and designed the experiments; Y.Z. led the experiments (with assistance from B.W., H.H., Z.W., S.L., C.Y., H.L., P.N., K.C., K.S., X.C., J.T., B.C. and S.E.); H.H. and Z.W. led the PCB designing; S.L. and C.Y. led the simulation; Y.Z., B.W., H.H., Z.W., S.L., C.Y., H.L., P.N., K.C., K.S., X.C., J.T. and S.E. contributed to data analysis and interpretation; Y.Z., B.W., H.H., S.L., C.Y. and S.E. drafted the manuscript and all authors provided feedback. Y.Z. and B.W. contributed equally to this work. S.E. supervised the study.

Competing interests: The authors declare no competing interests.

Data and materials availability: All data needed to evaluate the conclusions in the paper are present in the paper and/or the Supplementary Materials. Additional data related to this paper may be requested from the authors.

Figures and Tables

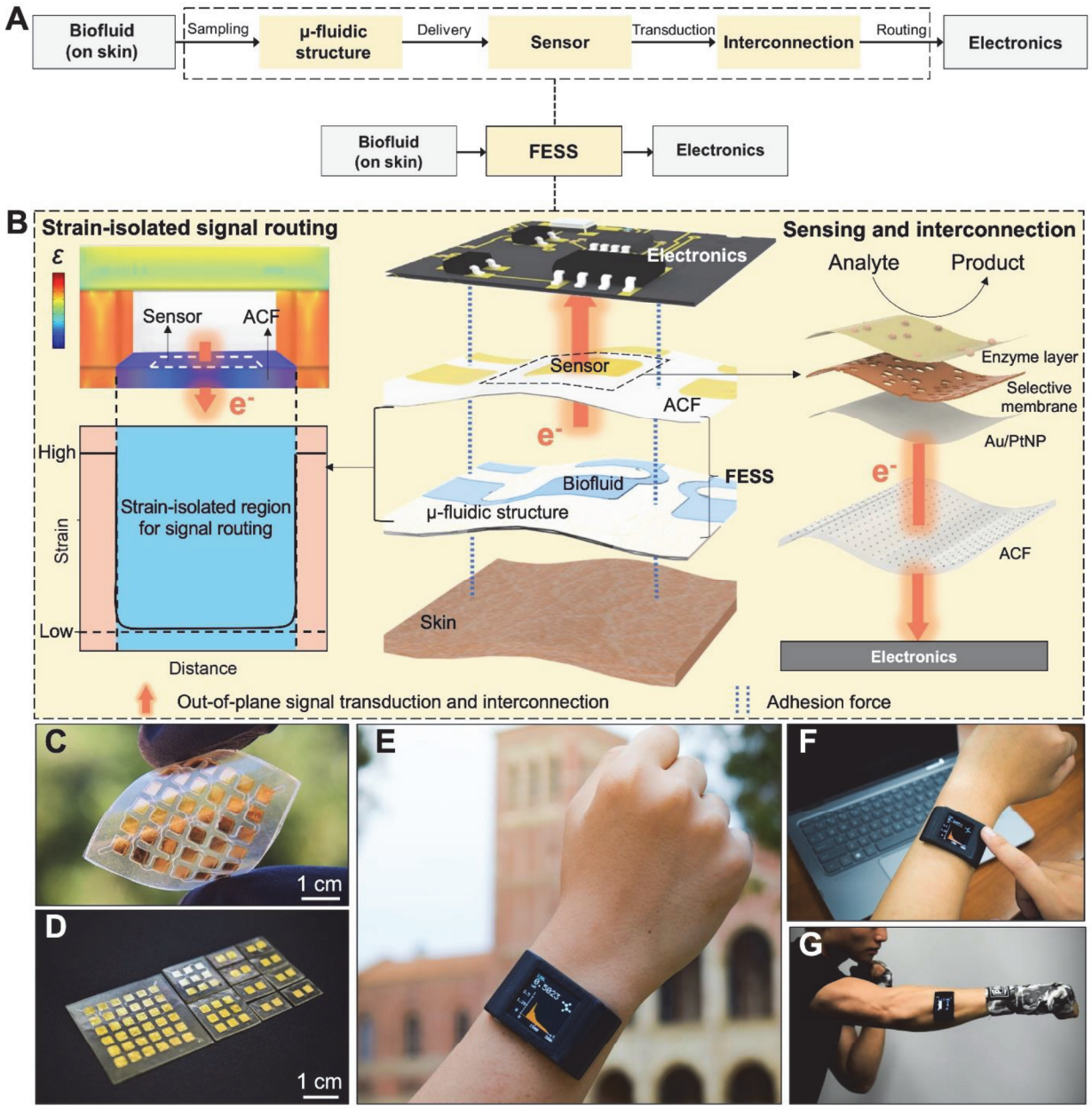

Fig. 1. Freestanding electrochemical sensing system (FESS) design rationale, implementation, and application. (**A**) Schematic of the biomarker information delivery pathway enabled by the FESS, illustrating sampling, sensing, and routing of epidermally-retrieved biomarker information to readout electronics through a single entity. (**B**) Design rationale of the FESS. (**C**) A representative implementation of the FESS, demonstrating flexibility and no in-plane interconnection. (**D**) A representative family of FESS devices, containing 1 × 2, 3 × 3 and 6 × 6 electrode arrays. (**E**) Custom-developed and FESS-enabled smartwatch for biomarker monitoring. (**F**, **G**) Deployment of the FESS-enabled smartwatch in stationary (**F**) and high intensity exercise (**G**) settings. Photo credit: Peterson Nguyen, Kaili Chiu, Yichao Zhao, University of California, Los Angeles.

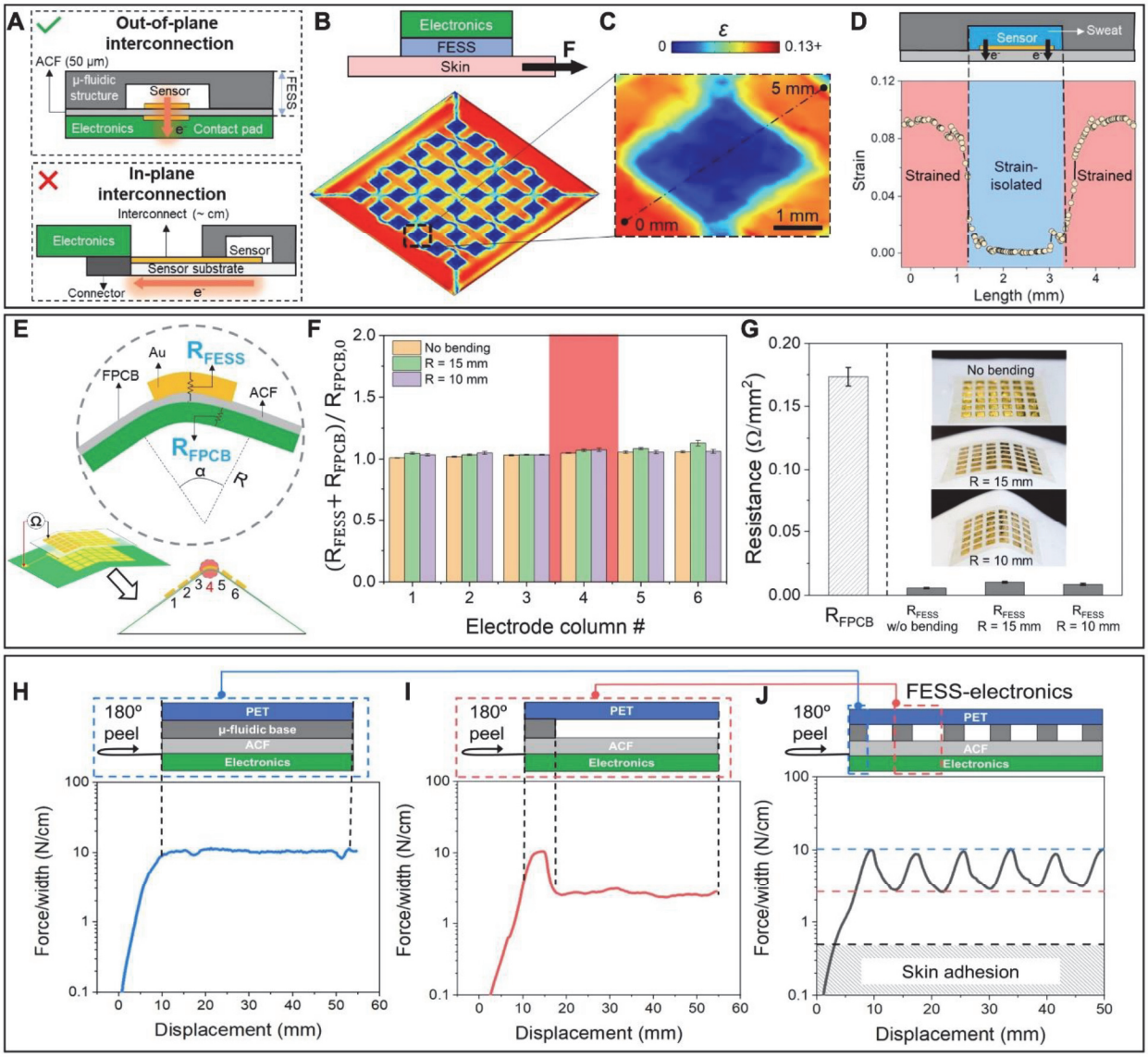

Fig. 2. FESS strain simulation and characterization of strain-isolated signal interconnection. (**A**) Illustration of the FESS' out-of-plane signal interconnection *vs.* conventional in-plane signal interconnection. Conventional implementations are constrained to signal routing through highly strained regions, while the devised FESS allows for routing via near-zero strain regions. (**B**) COMSOL-simulated strain (ε) profile of a representative FESS in the presence of an externally applied shear force, illustrating near-zero strain at the bottom of the microchannel (*i.e.*, substrate-biofluid interface). (**C**) Corresponding zoomed-in view of the strain profile for one 'pixel'. (**D**) Strain distribution along the dashed line in Fig. 2c. (**E**) Out-of-plane interconnection electrical characterization of FESS, performed under different localized bending angles (for an array of 6 × 6 Au electrodes). (**F**) Interconnection resistances of the bent FESS-FPCB (R_{FESS}+R_{FPCB}), for different localized bending angles (normalized with respect to R_{FPCB} with no bending: $R_{FPCB,0}$). Error bars indicate standard error of measurements across the 6 electrodes within each column. (**G**) Resistance measurements of the FESS electrodes under different bending angles (n = 36), in relation to the FPCB contact pad resistance ($R_{FPCB,0}$). (**H-J**) 180° peeling tests characterizing the interconnection adhesion between the PCB and FESS with different backing structures: microfluidic base-ACF (**H**), microfluidic channel-ACF (**I**), and a representative microfluidic channel array-ACF (**J**). Photo credit: Peterson Nguyen, University of California, Los Angeles.

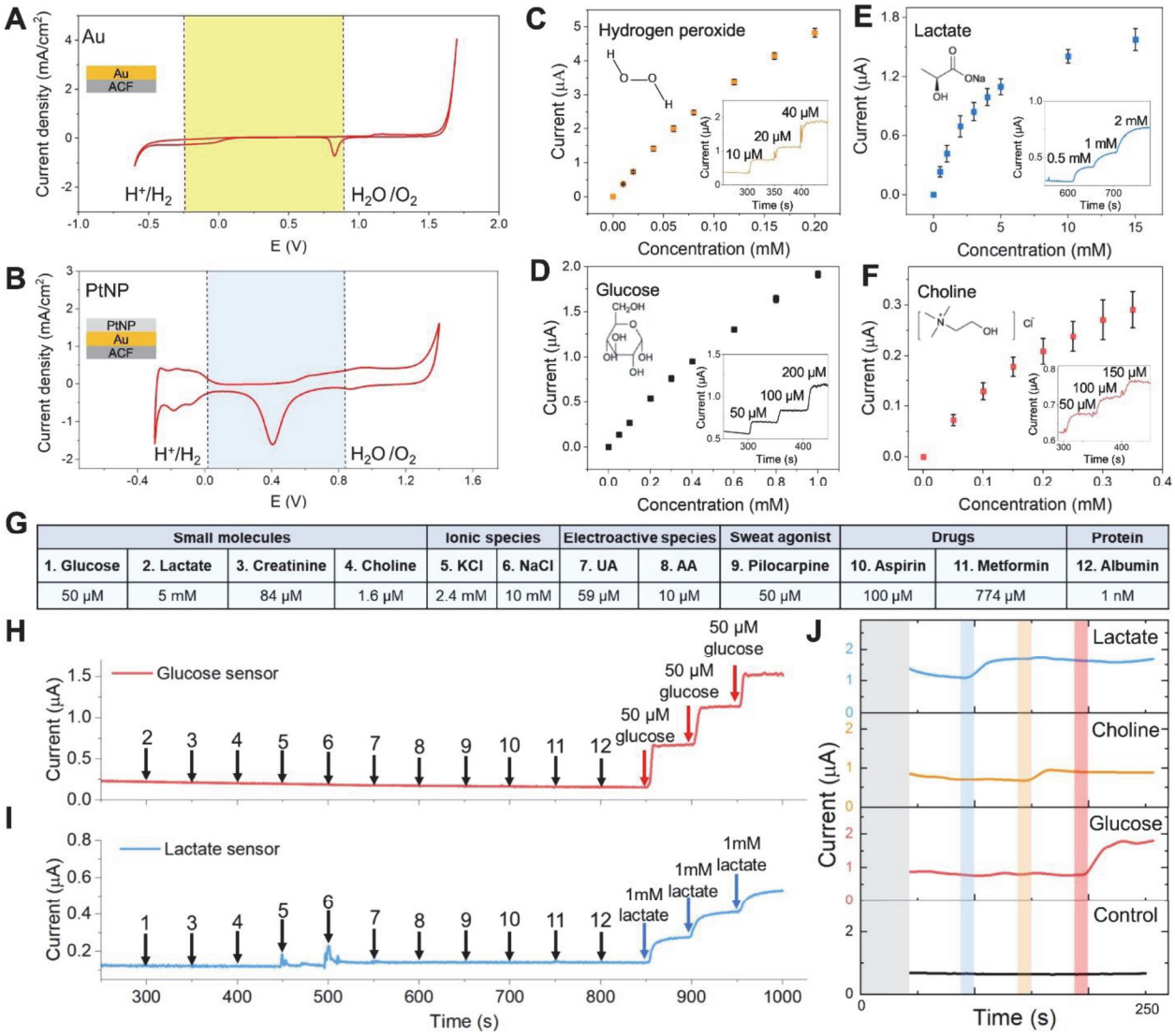

Fig. 3. **FESS signal transduction characterization.** (**A**, **B**) Cyclic voltammetry characterization of Au (**A**) and Au/PtNP (**B**) electrode surfaces of the FESS, performed in 0.1 M H_2SO_4. Stable operational potential window (*29*) is highlighted with the shaded background. (**C**-**F**) FESS-based hydrogen peroxide (**C**), glucose (**D**), lactate (**E**), and choline (**F**) sensor responses to the target analytes (error bars indicate standard error (SE), n = 3). Inset figures show representative amperometric responses. (**G**) Table of common interferents in biofluids (*e.g.*, sweat). (**H**, **I**) Comprehensive selectivity studies for glucose (**H**) and lactate sensors (**I**) by monitoring the corresponding sensor responses to the sequential introduction of the listed interferents and target analytes (the introduction timepoints and the interferents/target analytes are indicated by arrows). (**J**) Characterization of a representative sensor array response built on the FESS platform for multiplex sensing.

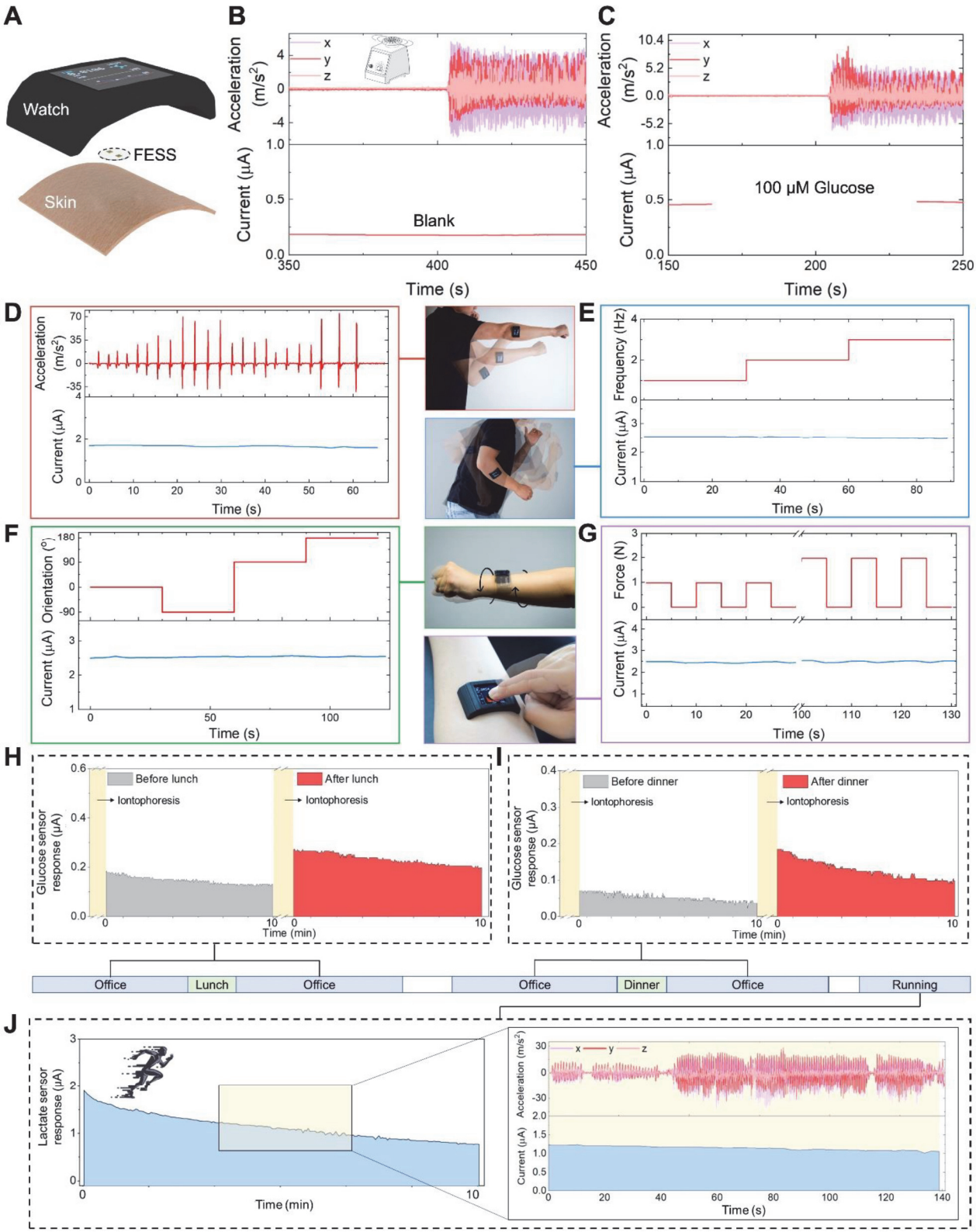

Fig. 4. Custom-developed FESS-integrated smartwatch for on-body application. (**A**) Illustration of the FESS-enabled smartwatch (containing FESS, LCD screen, PCB, and battery units housed within a 3D-printed case). (**B**, **C**) *Ex-situ* characterization of the FESS-PCB glucose sensing system response upon vortical vibration (FESS electrode: 6 mm^2, microfluidic channel height: 170 μm and volume: 4 μL). The vibrational acceleration profiles are presented in the top- half, and the sensor responses are captured in the bottom-half when tested in PBS (**B**) and 100 μM glucose in PBS (**C**). (**D-G**) On-body signal fidelity characterization of a FESS-PCB lactate sensing system

908 with a subject performing shadow boxing (**D**), arm swinging (**E**), wrist twisting (**F**), and device-
909 pressing (**G**). The acceleration, frequency, orientation, and force profiles are presented in the top-
910 half and sensor responses are captured in the bottom-half. (**H-J**) Monitoring the subjects' metabolite
911 profiles through various daily events and in different settings. Iontophoretically-induced sweat
912 glucose were measured before and after lunch (**H**) and dinner (**I**). (**J**) Sweat lactate measurements
913 during exercise (a representative motion-induced acceleration profile is shown on the right). Photo
914 credit: Peterson Nguyen, Kaili Chiu, Yichao Zhao, University of California, Los Angeles.
915

SUPPLEMENTARY MATERIALS

A Wearable Freestanding Electrochemical Sensing System

Authors

Y. Zhao[1,2†], B. Wang[1†], H. Hojaiji[1], Z. Wang[1], S. Lin[1], C. Yeung[1,2], H. Lin[1], P. Nguyen[1,3], K. Chiu[1,3], K. Salahi[1], X. Cheng[1,2], J. Tan[1,2], B. A. Cerrillos[1], S. Emaminejad[1*]

Affiliations

[1]Department of Electrical and Computer Engineering, University of California, Los Angeles, CA, USA.
[2]Department of Materials Science and Engineering, University of California, Los Angeles, CA, USA.
[3]College of Letters and Sciences, University of California, Los Angeles, CA, USA.
[*]Correspondence and requests for materials should be addressed to S.E. (emaminejad@ucla.edu)

Supplementary figures

Fig. S1. Bio-inspired *in-situ* sensing and signal interconnection.
Fig. S2. Design and fabrication of FESS components.
Fig. S3. Liner exchange procedure for the FESS construction.
Fig. S4. Visualization of the microfluidic module of the FESS and its integration with skin and electronics.
Fig. S5. Visualization of the FESS-skin reliable adhesion.
Fig. S6. Mechanical strain simulation of different implementations.
Fig. S7. The effect of mechanical deformation on the FESS electrical interconnection (ACF) resistance.
Fig. S8. Skin adhesive peeling test.
Fig. S9. Electrochemical properties of Au and Au/PtNP electrode surface of the FESS.
Fig. S10. FESS-based electrochemical sensor accuracy validation.
Fig. S11. Anti-corrosion property of the FESS in aqueous environment.
Fig. S12. FESS-enabled smartwatch.
Fig. S13. *Ex-situ* characterization of the signal stability of FESS-PCB glucose sensing system in presence of vortical vibration.
Table S1. Structural composition of FESS.
Table S2. Chemical composition of FESS sensing interface.
Movie S1. ACF-based interconnection under mechanical deformation.

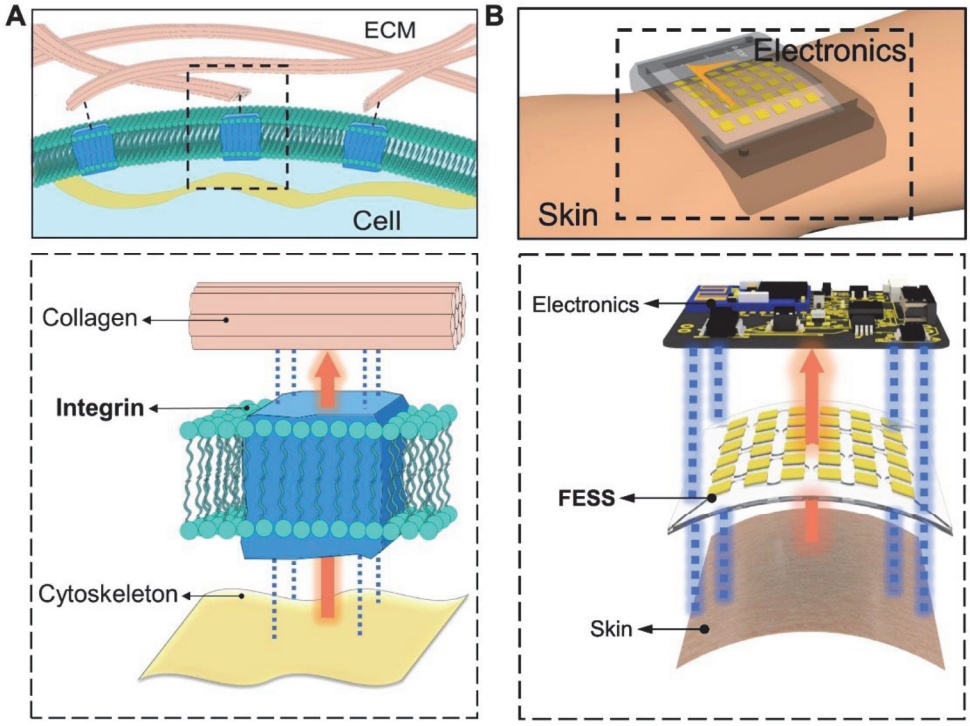

Fig. S1. Bio-inspired *in-situ* sensing and signal interconnection. (A) Conceptual illustration of the physiological information exchange between intracellular/extracellular matrices facilitated by cell adhesive molecules (integrin) via sensing, out-of-plane signal interconnection, and double-sided adhesion. **(B)** *In-situ* sensing, out-of-plane signal interconnection, and double-sided adhesion enabled by FESS, as a single entity, placed between skin and electronics.

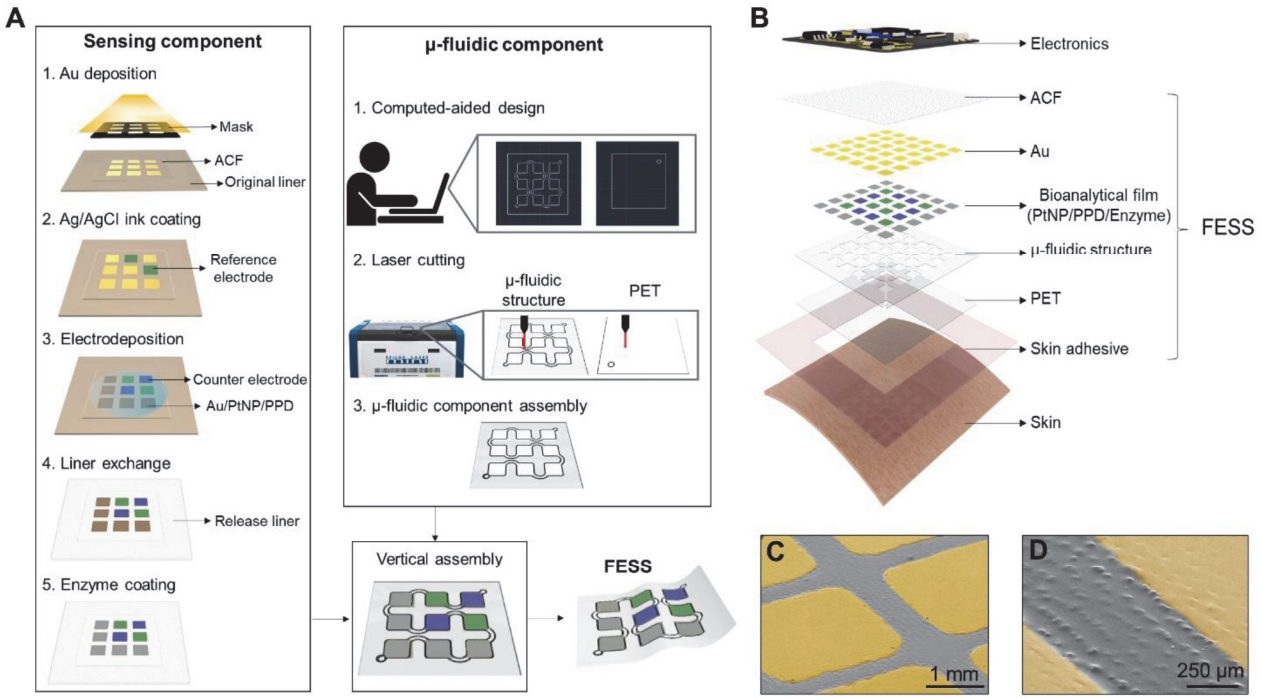

Fig. S2. Design and fabrication of FESS components. (**A)** The design and fabrication processes of the sensing and microfluidic components of the FESS. The liner exchange step is visually detailed in Fig. S3. **(B)** Exploded view of the FESS. **(C)** SEM image of Au electrodes patterned on the ACF layer. **(D)** The zoom-in view of the electrode-patterned ACF layer.

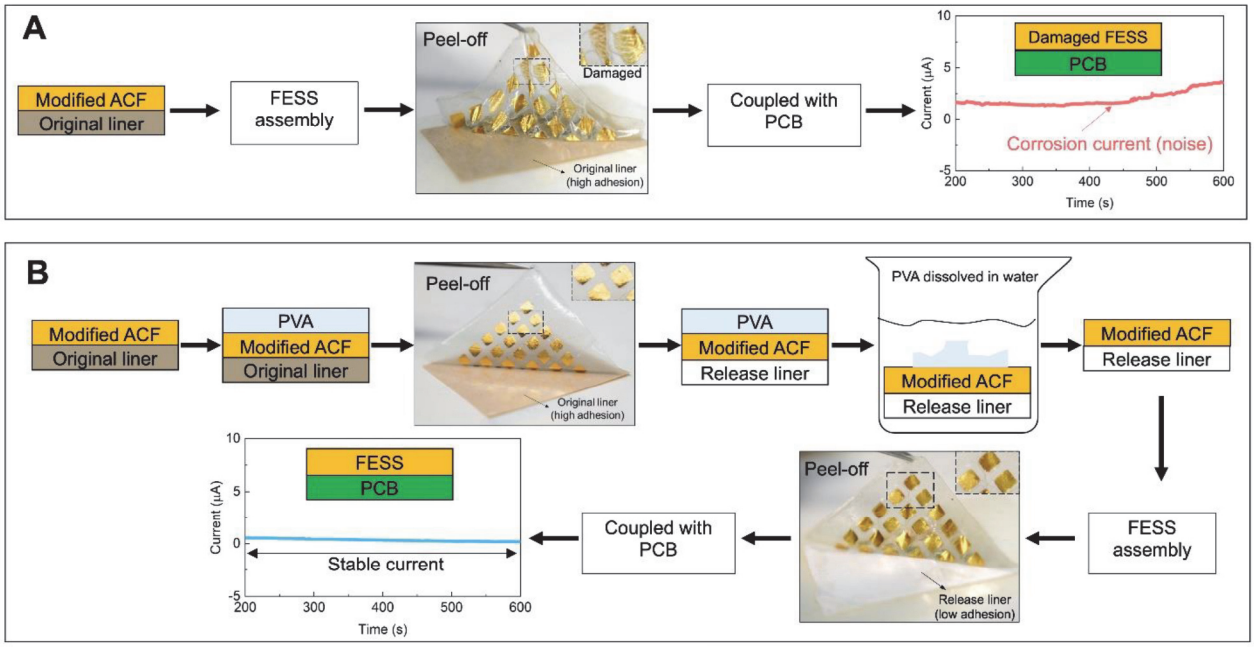

Fig. S3. Liner exchange procedure for the FESS construction. (**A**) Demonstration of the device- and operational-level failure of the FESS (constructed without following the devised liner exchange procedure). The FESS is deformed during peeling from the original liner due to the high level of FESS-liner adhesion. The presence of the defects formed on the FESS electrodes subsequently leads to the corrosion of the underlying PCB contact pads, as evident from the unstable amperometric recording of the FESS-coupled PCB (performed in PBS, 0.5 V *vs.* Ag/AgCl). (**B**) Demonstration of the preserved device- and operational integrity of the FESS (constructed following the devised liner exchange procedure). Here, water soluble PVA layer is used as a backing to facilitate the liner exchange, replacing the original liner with a low adhesion release liner. The preserved operational integrity of the FESS is validated by performing amperometry and recording stable background current (performed in PBS, 0.5 V *vs.* Ag/AgCl). Photo credit: Peterson Nguyen, University of California, Los Angeles.

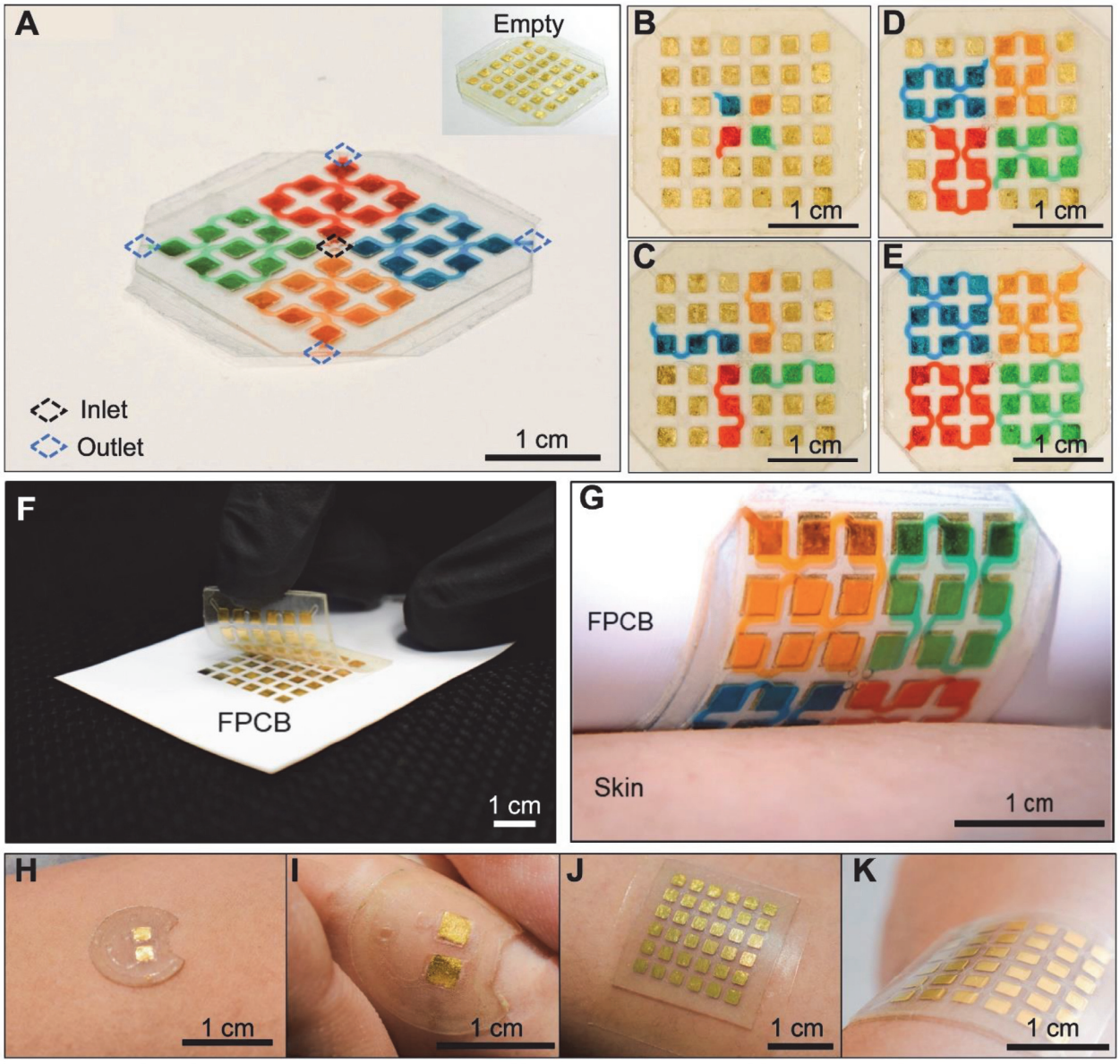

Fig. S4. Visualization of the microfluidic module of the FESS and its integration with skin and electronics. (A) A representative 6×6-pixel FESS, filled with dye-colored solution to visualize its microfluidic network. Inset shows the corresponding unfilled FESS. **(B)-(E)** Optical images of the FESS as it is progressively filled. **(F)** Integration of a representative 6×6-pixel FESS with FPCB via adhesion force. **(G)** Adherence of the FESS-FPCB with skin via adhesion force. **(H)-(K)** A representative 1×2-pixel and 6×6-pixel FESS modules adhered to flat/curved skin. Photo credit: Peterson Nguyen, University of California, Los Angeles.

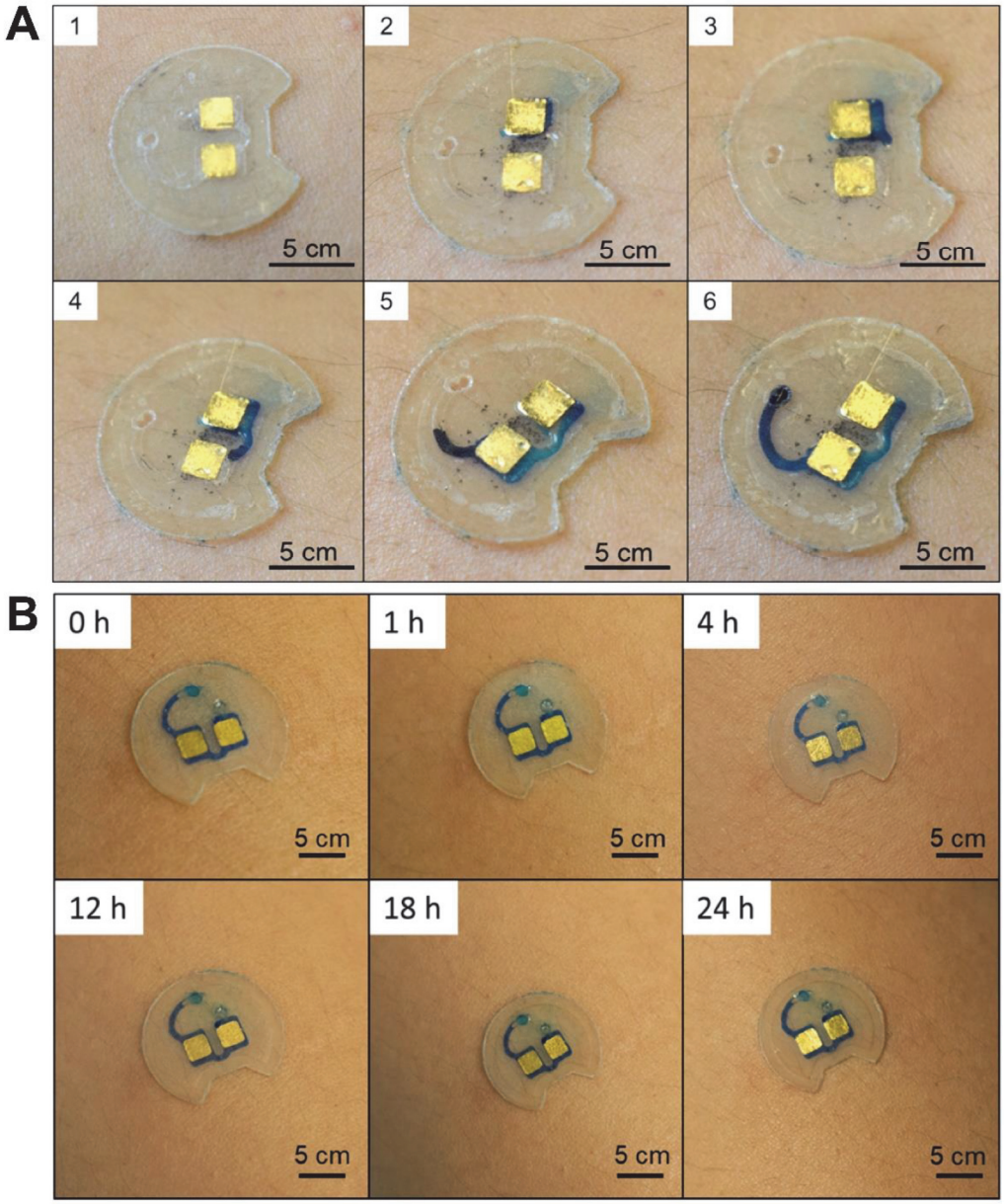

Fig. S5. Visualization of the FESS-skin reliable adhesion. (A) Sequential optical images of a representative FESS (microfluidic channel volume: 4 μL), adhered to the forearm of a subject (engaged in physical exercise), indicating the leakage-free progression of secreting sweat in the FESS (imaged over a 10-min window). **(B)** Demonstration of FESS-skin long-term adhesion performed on the forearm of a subject (engaged in routine daily activities) over 24 hours. The FESS was filled with blue-dyed PBS and sealed with epoxy to visualize the microfluidic channel. Photo credit: Peterson Nguyen, University of California, Los Angeles.

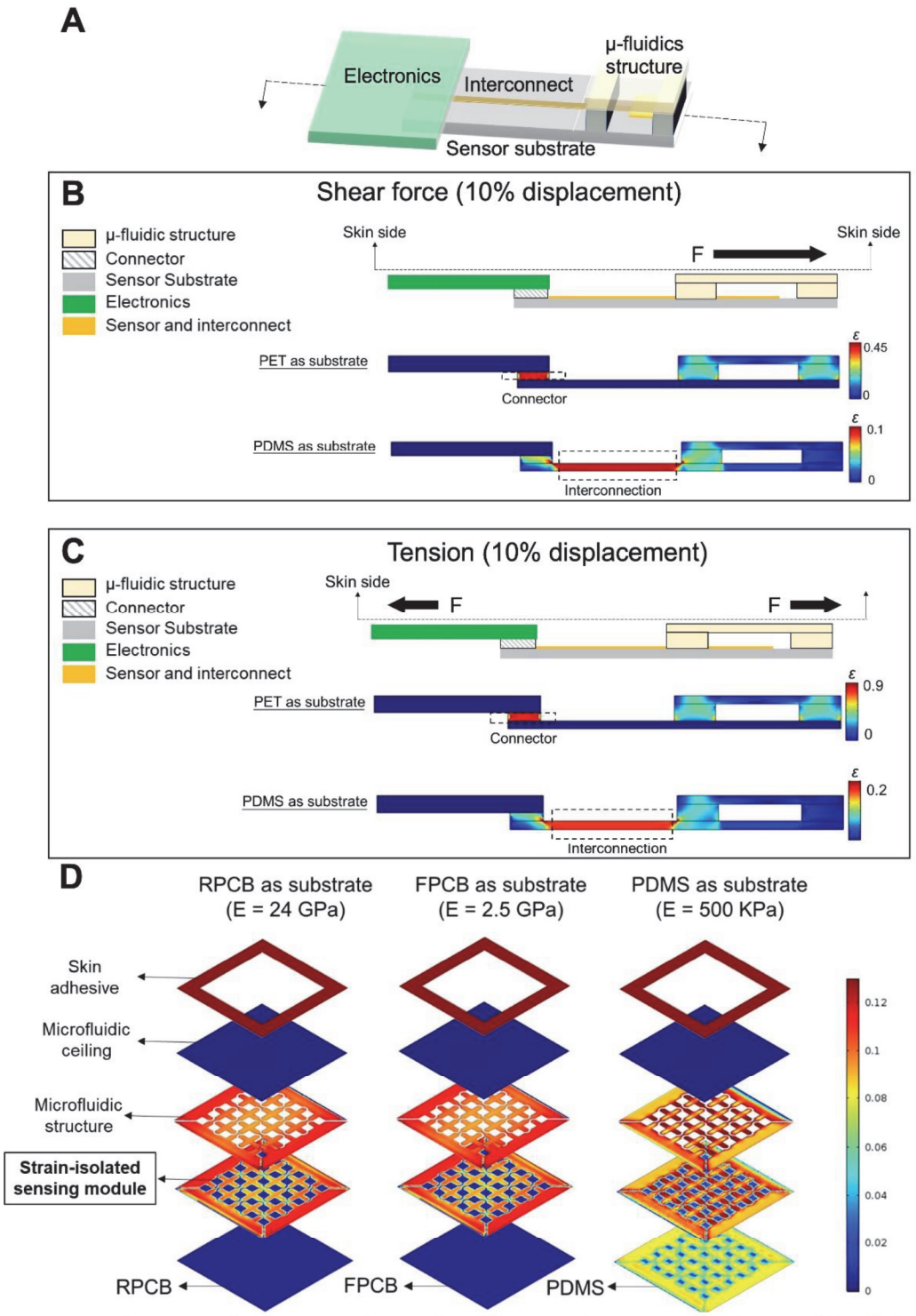

Fig. S6. Mechanical strain simulation of different implementations. (A) Schematic of conventional in-plane interconnection between sensor and electronics. **(B), (C)** COMSOL-simulated strain profile of sensor-electronics systems implemented with in-plane interconnections and rigid connectors under shear (**B**) and tension (**C**). Both cases of flexible (PET) and stretchable (PDMS) substrates are considered for the sensor substrate. **(D)** COMSOL-simulated strain profiles experienced by different layers of a representative FESS and in the presence of a shear force. Three different electronics substrate materials are considered: PDMS, polyimide (PI), and Flame retardant 4 (FR4) with corresponding Young's modulus: 500 kPa, 2.5 GPa, and 24 GPa.

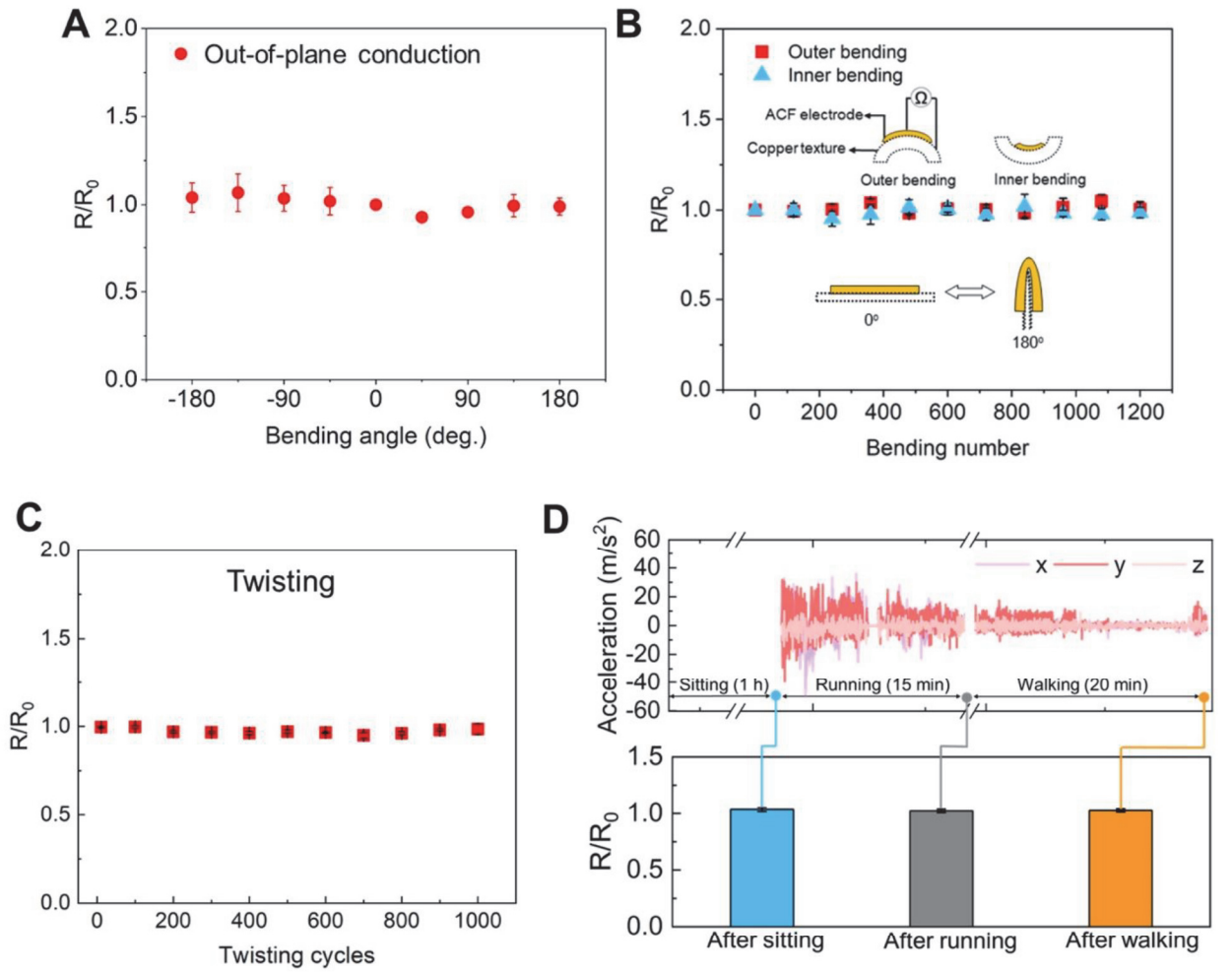

Fig. S7. The effect of mechanical deformation on the FESS electrical interconnection (ACF) resistance. (A) Interconnection resistance measurements at different bending angles (SE, n = 3). **(B)** Cyclical interconnection resistance measurements involving repeated 0-to-180° bendings, where the interconnection resistance was probed after each bending under 180° (error bars indicate SE, n = 3). Inset shows the set-up for probing ACF-based electrode, which was adhered onto a conductive copper texture. **(C)** Cyclical interconnection resistance measurements involving repeated twisting, where the interconnection resistance was probed (using ACF adhered onto an FPCB) after manual twisting (twisting angle ~ 90°, error bars indicate SE, n = 3). See Movie S1 for the manual experiment procedure. **(D)** Interconnection resistance measurements before/after different daily activities (the recorded acceleration profile during the running and walking activities are presented atop). R represents the measured interconnection resistance and R_0 represents the measured interconnection resistance at the initial (undeformed) state.

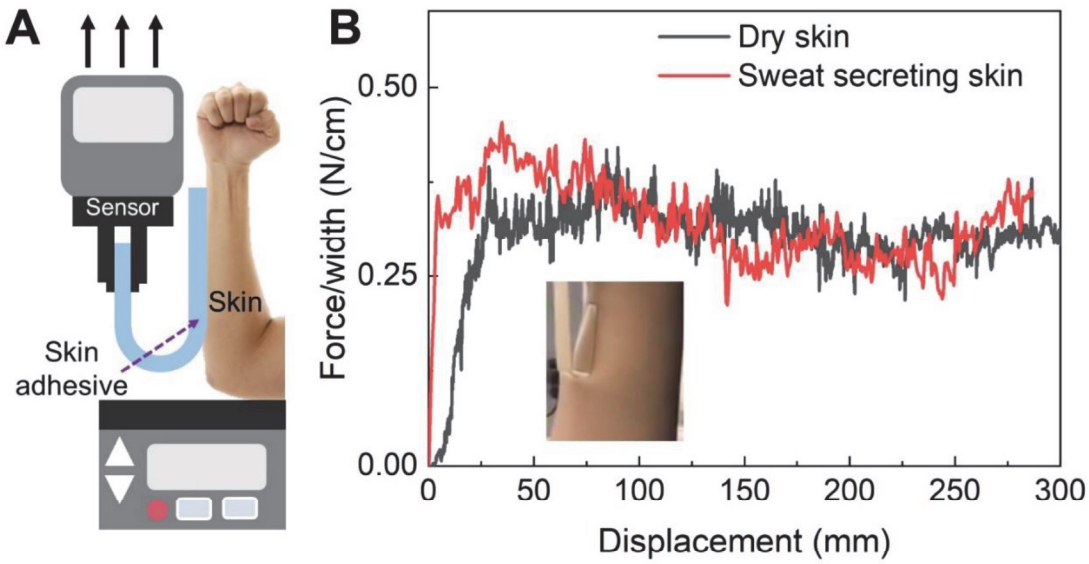

Fig. S8. Skin adhesive peeling test. (**A**) 180° peeling adhesion force characterization setup using Instron 5943. (**B**) Adhesion force characterization for the skin adhesive-skin interface performed on dry and exercise-induced sweat secreting skin (where the skin adhesive was adhered to skin prior to physical exercise), indicating similar strength of adhesion between the skin and skin adhesive for both conditions.

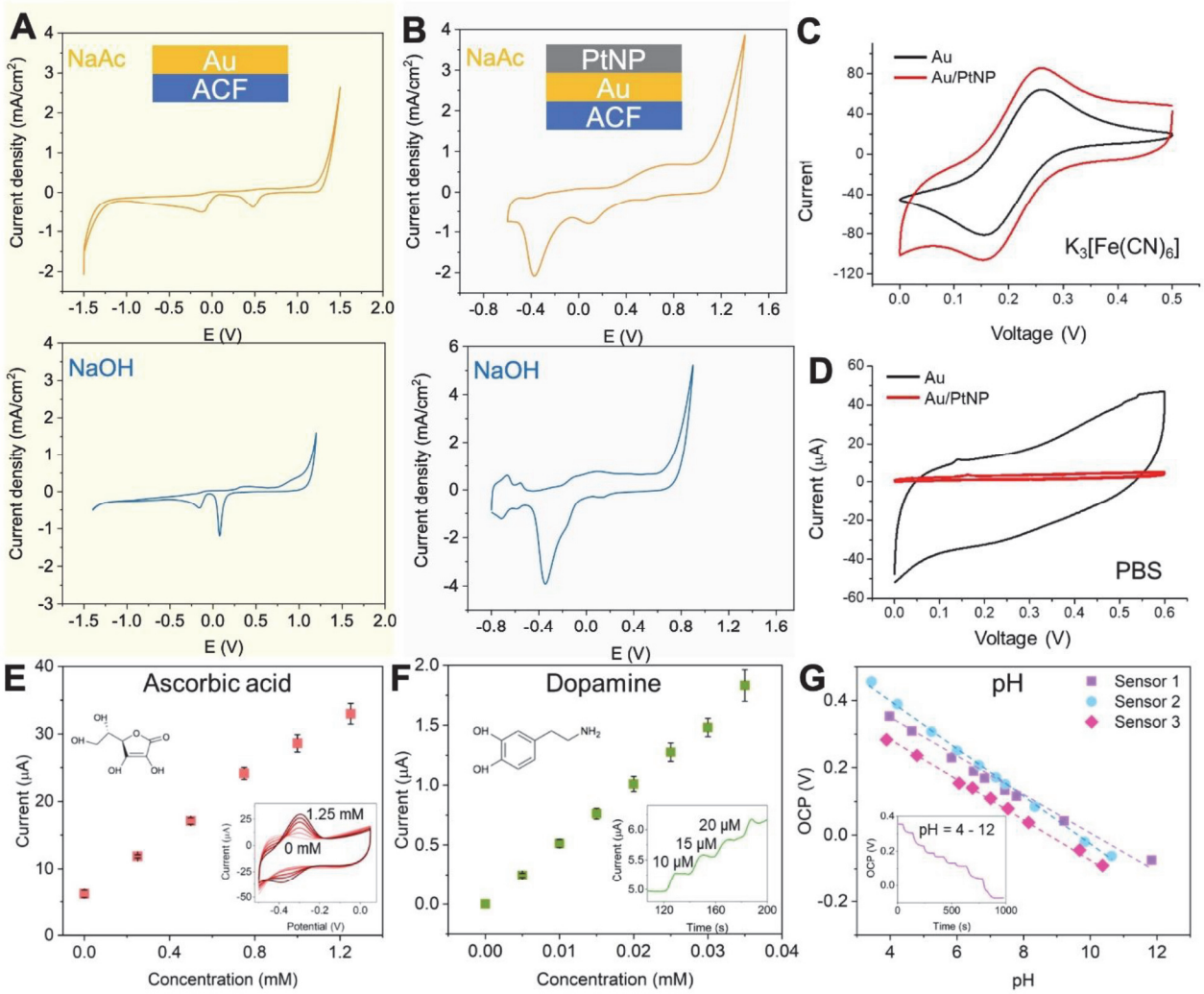

Fig. S9. Electrochemical properties of Au and Au/PtNP electrode surface of the FESS. Cyclic voltammetry characterization of Au **(A)** and Au/PtNP **(B)** electrode surfaces of the FESS in 0.1 M NaAc (pH ~7.5), and 0.1 M NaOH (pH ~13) solutions. Cyclic voltammetry characterization of Au and Au/PtNP electrode surfaces of the FESS in 5 mM $K_3[Fe(CN)_6]$ + 0.1 M KCl (**C**) and 0.1 M PBS (**D**) solutions. FESS-based Au/PtNP electrode responses (SE, n = 3) toward dopamine (**E**) and ascorbic acid (**F**). **(G)** FESS-based pH sensors' calibration curves (SE, n = 3).

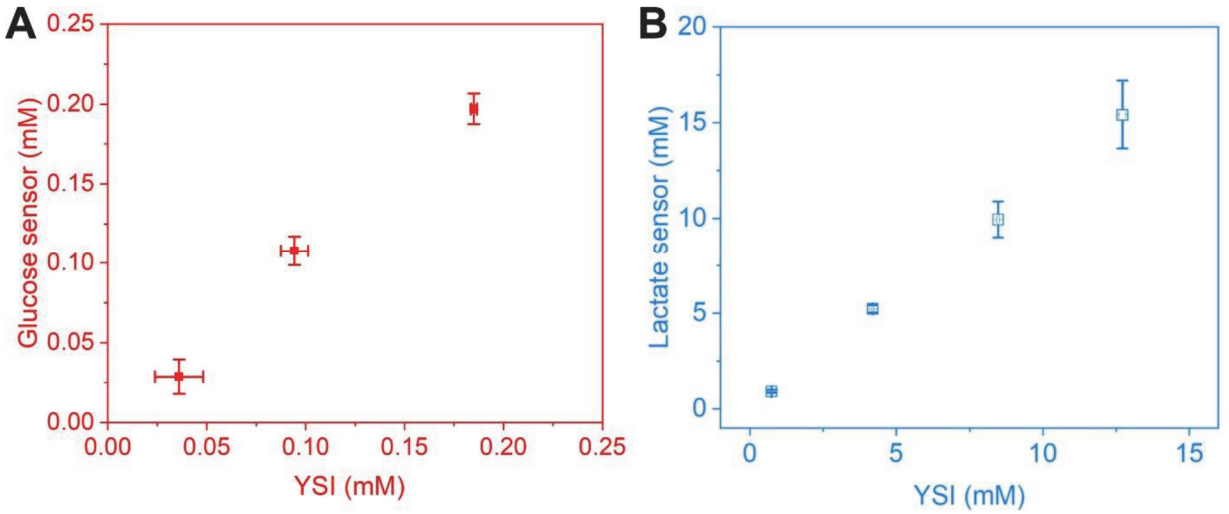

Fig. S10. FESS-based electrochemical sensor accuracy validation. Glucose **(A)** and lactate **(B)** concentration measurements in a random sequence by FESS-based glucose (SE, n = 3) and lactate sensors *vs.* a gold-standard benchtop biochemistry analyzer (YSI 2900D, SE, n = 3).

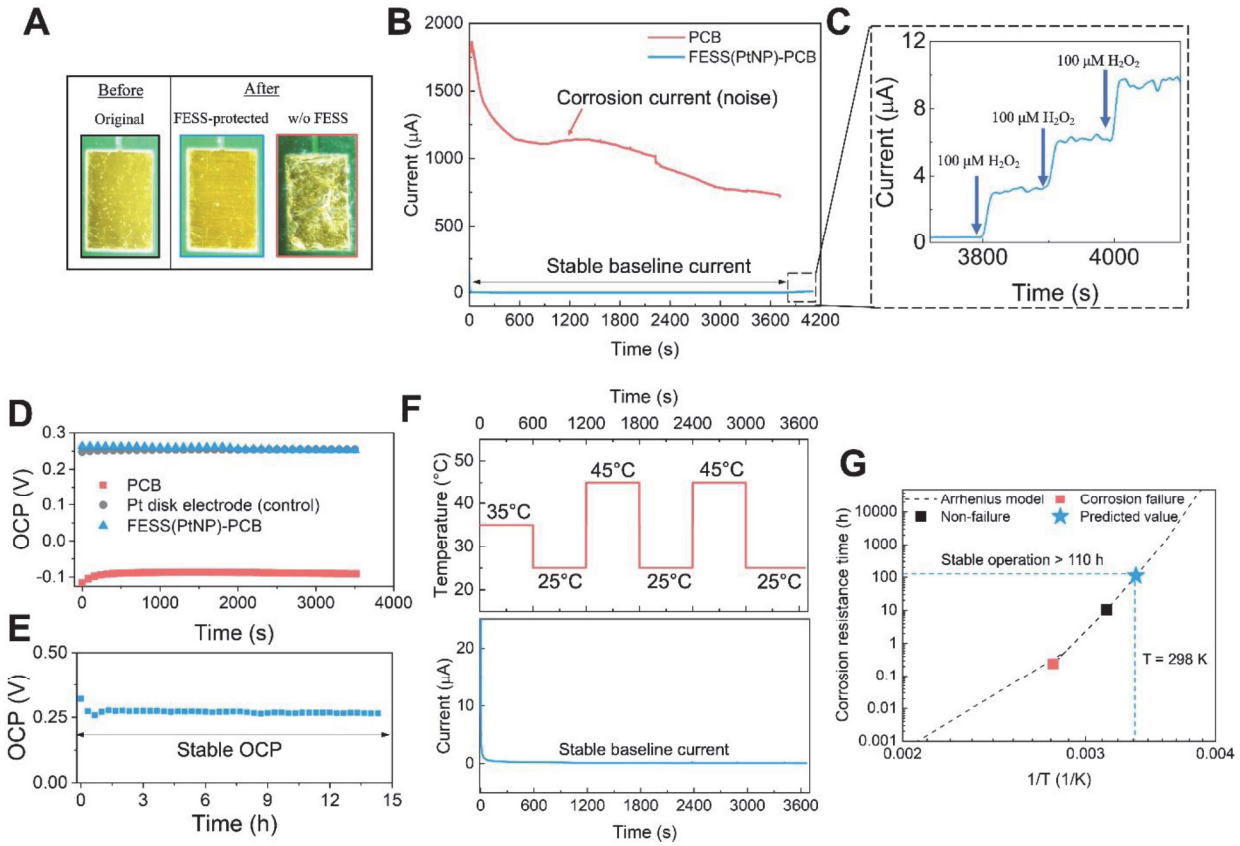

Fig. S11. Anti-corrosion property of the FESS in aqueous environment. **(A)** Optical images of the two cases of FESS (PtNP)-coupled (image taken post-peeling) and bare PCB contact pads upon performing amperometric measurements (with contact pads immersed into PBS, 0.5 V *vs.* Ag/AgCl for 1 hour). The original optical image of the bare PCB contact pad is included for comparison. **(B)** Amperometric recordings performed with FESS(PtNP)-coupled and bare PCB contact pads (in PBS, 0.5 V *vs.* Ag/AgCl). The measured significantly large current density of the bare contact pad case indicates the onset of the electrochemical corrosion. **(C)** The follow up measured FESS (PtNP)-coupled electrode's linear responses to oxidant (H_2O_2) indicate the preserved catalytic capabilities of the electrodes (performed after the corrosion characterization experiment, shown in **B**). **(D)** Open circuit potential (OCP) measurement of bare and FESS (PtNP)-coupled PCB contact pads as well as standard Pt disk electrode for 1 hour in PBS against a standard Ag/AgCl reference electrode. The comparable performance of the FESS (PtNP)-coupled and Pt disk electrode cases indicate the transformation of the PCB contact pads to Pt-based electrodes upon coupling of the FESS (PtNP) with PCB contact pads. **(E)** OCP measurement of the FESS (PtNP)-coupled PCB contact pads over 14 hours, indicating the high stability of FESS (PtNP)-coupled interface for long-term operation in aqueous solution. **(F)** Amperometric recording of FESS (PtNP)-coupled PCB electrode in PBS (0.5 V *vs.* Ag/AgCl), during thermal cycling. **(G)** Accelerated life testing (PBS, 0.5 V *vs.* Ag/AgCl, heated with hot plate) to predict the minimum corrosion resistance lifetime of FESS (PtNP)-coupled PCB contact pads at room temperature (298.15 K) using Arrhenius model. The fitting is based on two reference measurements, performed at: 1) 358.15 K (leading to corrosion) and 2) 318.15 K, which did not lead to corrosion during the recorded time window (where stable recorded amperometric current was measured), and thus, used to set the lower-bound on the estimated lifetime for stable operation at room temperature.

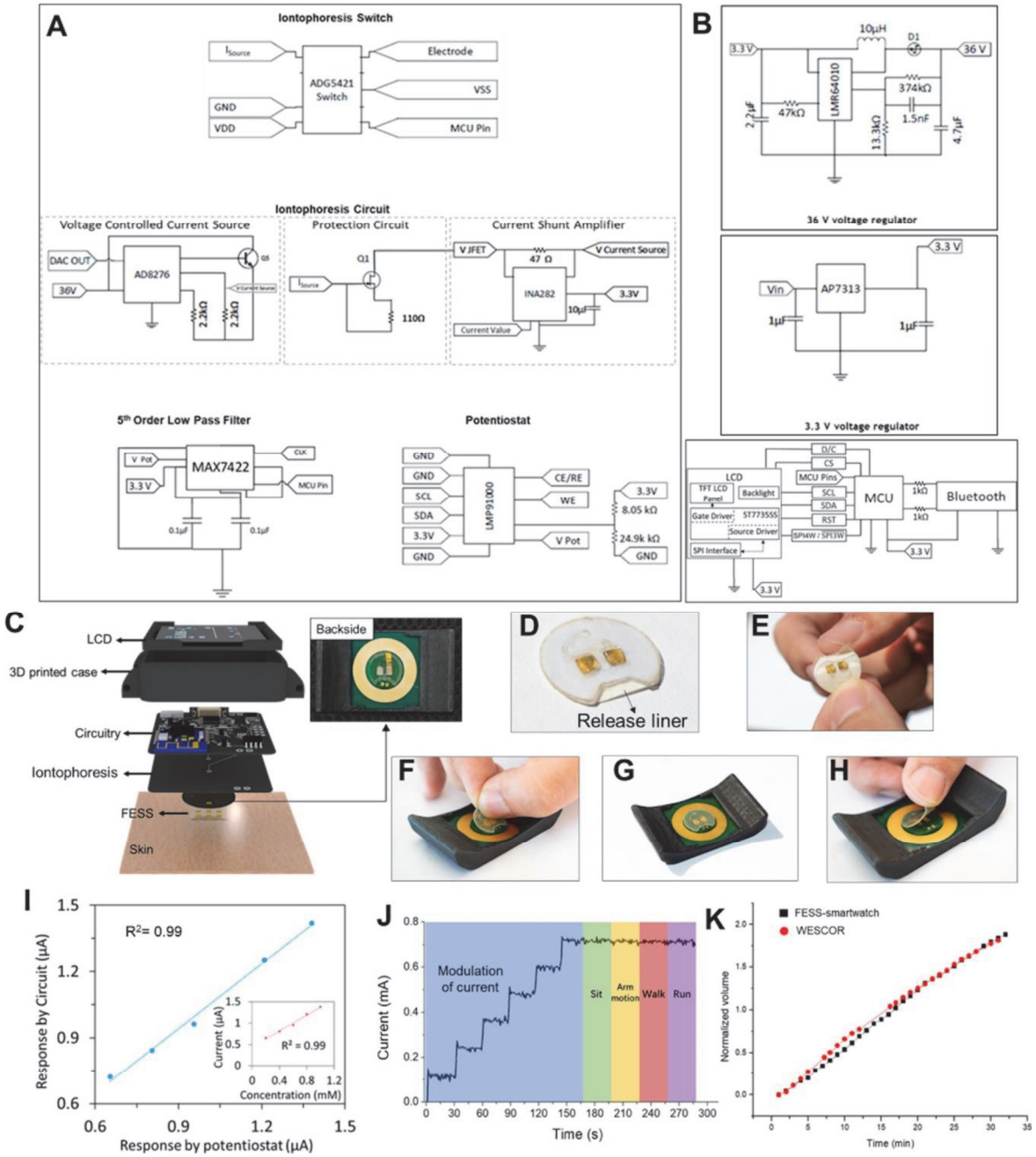

Fig. S12. FESS-enabled smartwatch. (A) Schematic diagrams of the switch, programmable iontophoresis, and sensing circuitries. **(B)** Schematic diagrams of the implemented power-regulating/MCU/LCD/Bluetooth circuitries. **(C)** Exploded view of the custom-developed wearable smartwatch with a ring-shaped iontophoresis module. The backside of the smartwatch is shown on the right, illustrating the interface of the smartwatch readout contact pads with the FESS (at the center). **(D)-(H)** Picking, placing, and detaching a representative FESS (1×2-pixel, 6 mm^2 electrode) on the back of the custom-developed smartwatch. **(I)** The measured amperometric glucose sensor response by PCB *vs*. potentiostat (inset shows the corresponding calibration curve obtained by the potentiostat). **(J)** Mobile application-based controlled delivery of different iontophoresis current levels. **(K)** Comparison of the secreted sweat volume (normalized with respect to the stimulated area) induced by the FESS-smartwatch iontophoresis module *vs*. a commercial iontophoresis instrument (WESCOR). Photo credit: Peterson Nguyen, University of California, Los Angeles.

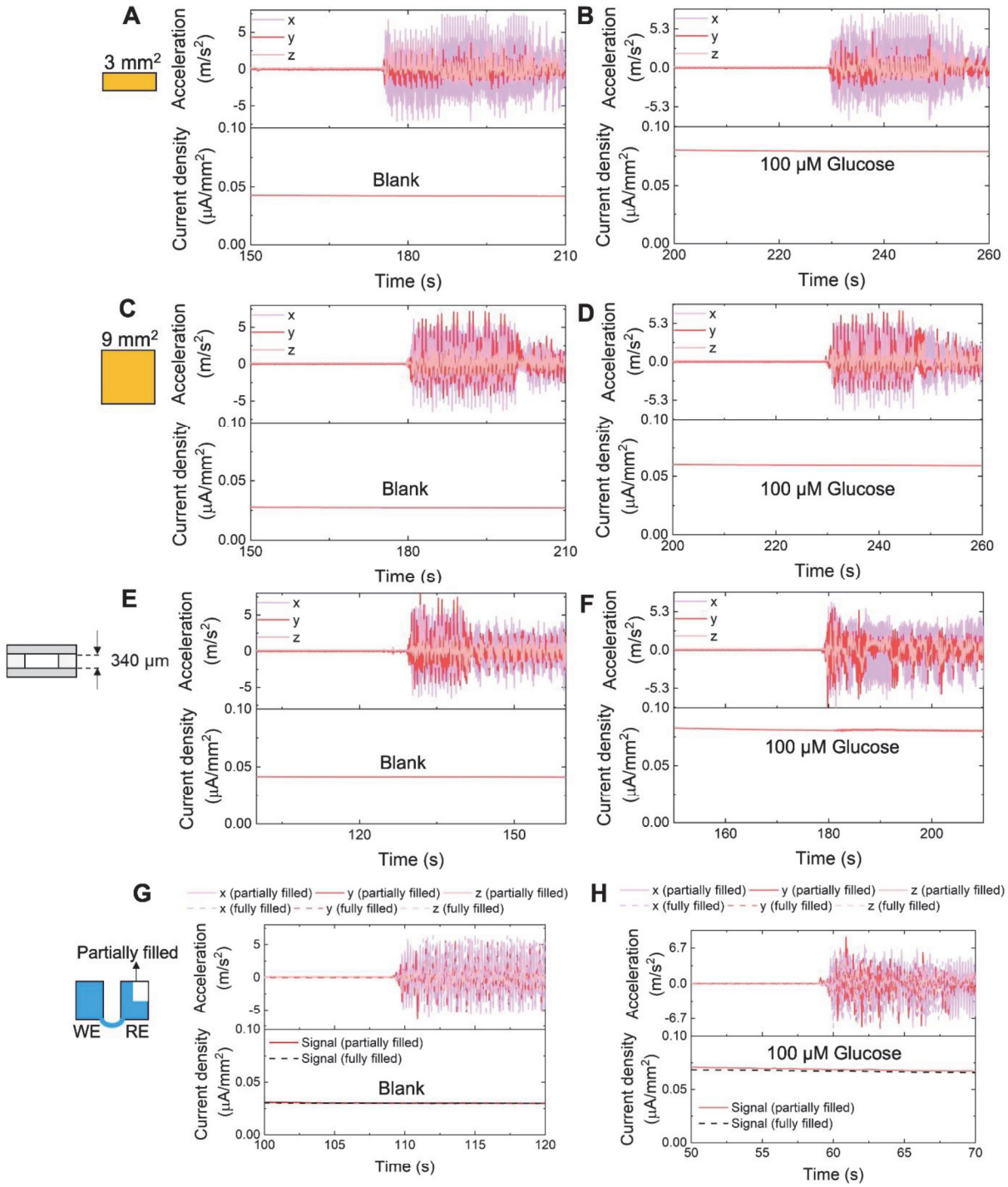

Fig. S13. *Ex-situ* characterization of the signal stability of FESS-PCB glucose sensing system in presence of vortical vibration. The measured amperometric responses of FESS to blank solution and 100 μM glucose solution with 3 mm^2 (**A, B**) and 9 mm^2 FESS-electrodes (**C, D**) (both with channel height: 170 μm), as well as with FESS channel height of 340 μm (**E, F**) (6 mm^2 electrode). Amperometric response of FESS to blank solution (**G**) and 100 μM glucose solution (**H**), where the FESS microfluidic channel (height: 170 μm) was partially filled (~ 90%) with the solution (while ensuring that the 6 mm^2 working electrode, WE, was fully covered with the solution and fluidically connected to partially covered 6 mm^2 reference electrode, RE, mimicking the initial progression of sweat in the designed device where WE will be reached first, prior to RE). The corresponding vibrational acceleration profiles is shown atop each amperometry recording.

Table S1. Structural composition of FESS

Materials	Function	Young's modulus	Thickness	Adhesion type
Anisotropic adhesive film	Sensing electrode and microfluidic channel substrate/vertical signal transduction	450 MPa	50 μm	Double-sided adhesion/acrylic-based
Double-sided adhesive tape	Microfluidic wall (surrounding the biofluid)	450 MPa	170 μm	Double-sided adhesion/acrylic-based
Polyethylene terephthalate	Microfluidic ceiling	24 GPa	100 μm	N/A
Skin adhesive tape	Skin adhesion	450 MPa	170 μm	Double-sided adhesion/acrylic-based

Table S2. Chemical composition of FESS sensing interface

Chemical name	Deposition method	Function/Role
Gold (Au)	E-beam deposition	Electron transfer
Platinum nanoparticle (PtNP)	Electrodeposition	Electrochemical catalyst/electron transfer
Poly(m-phenylenediamine)	Electrodeposition	Selective membrane
Enzymatic layer (Glucose-, lactate-, choline oxidase)	Drop casting	Glucose catalyst (enzyme activity: 100-250 units/mg) Lactate catalyst (enzyme activity: ~100 units/mg) Choline catalyst (enzyme activity: ≥10 units/mg)
Chitosan	Drop casting	Enzyme immobilization
Polyvinyl chloride (PVC)	Drop casting	Diffusion limiting layer (only for lactate sensor)